Explicit Brillouin Flow Solutions in Magnetrons, Magnetically Insulated Line Oscillators, and Radial Magnetically Insulated Transmission Lines

Y. Y. Lau, *Fellow, IEEE*, Drew A. Packard, *Member, IEEE*, Christopher J. Swenson, *Student Member, IEEE*, John W. Luginsland, *Fellow, IEEE*, Dion Li, *Student Member, IEEE*, Abhijit Jassem, Nicholas M. Jordan, *Senior Member, IEEE*, Ryan D. McBride, *Member, IEEE*, and Ronald M. Gilgenbach, *Life Fellow, IEEE*

Abstract—This article re-examines the Brillouin flow solutions in crossed-field diodes, with applications to magnetrons, magnetically insulated line oscillators (MILOs), and magnetically insulated transmission lines (MITLs). The Brillouin flow solutions are constructed for various geometries, including planar magnetrons, MILOs, and MITLs, cylindrical magnetrons with electrons flowing in the azimuthal direction, cylindrical MITLs and MILOs with electrons flowing in the axial direction, and radial MITLs and MILOs with electrons flowing in the radial direction. A common theme of this analysis is that two main external parameters are used to characterize the Brillouin flow: the anode–cathode voltage (V_a) and the total magnetic flux within the crossed-field diodes (A_a). These two parameters are equivalent to the gap voltage and a specification of the degree of magnetic insulation, which is approximately equal to the ratio of the magnetic field to the Hull cutoff (HC) magnetic field. The magnetic flux may be provided externally by a magnet (as in a magnetron) or by the wall currents without an external magnet (as in a MILO or MITL), or by some combination of the two, as in the intermediate case of a magnetron–MILO hybrid. Once these two parameters are specified, the electron flow speed at the top of the Brillouin hub is uniquely determined. This immediately yields the Buneman–Hartree (BH) condition according to the Brillouin flow model, whether it be a planar magnetron or a cylindrical MILO. In so doing, we have obtained, for the first time using the Brillouin flow model, the BH condition for a cylindrical MILO, and we show that the same condition is obtained from the single-particle orbit model. We also found that, in general, the electron current within the Brillouin hub contributes only to a very small fraction of the magnetic flux A_a, regardless of the gap voltage V_a, thereby correcting an erroneous notion that the electron flow within the crossed-field gap could be responsible for the magnetic insulation. Another counter-intuitive finding is that, for a given degree of magnetic insulation, the Brillouin hub height decreases as the gap voltage V_a increases. These conclusions, and other results, were based on the simple, explicit analytic expressions that we have obtained for the Brillouin flow profiles, including the velocity, electron density, as well as the self-magnetic field and the self-electric field profiles due to the Brillouin hub electrons. From these analytical expressions, we deduce useful scaling laws that are applicable to the prevailing cases where the magnetic field exceeds 1.5 times the HC magnetic field, and they are valid in both relativistic and non-relativistic regimes. Thus, these scaling laws show the contrast between magnetrons and MILOs, and a ready assessment of the viability of building a moderate-current MILO, a low-voltage MILO, and a magnetron–MILO hybrid which might combine the advantages of a magnetron and a MILO. The Brillouin flow profiles in a radial MITL are explicitly calculated. Additional issues are addressed.

Index Terms—Brillouin flow, crossed-field devices, magnetically insulated line oscillator (MILO), magnetically insulated transmission lines (MITLs), magnetron.

Y. Y. Lau, Drew A. Packard, Christopher J. Swenson, Dion Li, Abhijit Jassem, Nicholas M. Jordan, Ryan D. McBride, and Ronald M. Gilgenbach are with the Department of Nuclear Engineering and Radiological Sciences, University of Michigan, Ann Arbor, MI 48109 USA (e-mail: yylau@umich.edu).
John W. Luginsland was with Confluent Sciences, LLC, Albuquerque, NM 87111 USA. He is now with the Air Force Office of Scientific Research, Arlington, VA 22203 USA.

I. INTRODUCTION

MAGNETICALLY insulated line oscillators (MILOs) [1] and relativistic magnetrons (RMs) [2] are both crossed-field devices capable of generating high-power microwaves (HPMs) [3]–[31]. The RM has the same operating principles as the kilowatt-class magnetrons that power the microwave oven [32]–[35], but upgraded in power exceeding a million times [2]–[5]. The MILO is similar to the RM but does not require an external magnetic field. These two devices are thus very different, yet similar. The RM possesses a moderately high efficiency. The MILO has a much lower efficiency, but has tremendous system advantages as no external magnetic field is required, leading to a substantial reduction in size and weight compared with the RM.

Extensive literature on magnetrons has existed for over 70 years [32]–[35]. While MILOs have been in existence for more than 30 years, they are much less developed in comparison. For example, even the Buneman–Hartree (BH) condition,

which governs the operation of magnetrons, does not seem to have been properly established for the cylindrical MILO. One might also find confusing characterizations of the properties of the electron flows in a MILO. However, MILOs have received considerable attention recently [3], [4], [13]–[31], largely because their operation does not require an external magnetic field. The incomplete understanding of MILOs, in particular, how HPMs are generated in comparison with magnetrons, has greatly hindered efforts to find an optimal crossed-field configuration, if one exists, that might combine the advantages of MILOs and RMs. The viability of a low-voltage MILO is also attractive, because of the availability of low-impedance linear transformer drivers (LTDs) in recent years [36]–[39].

The above background motivated us to provide a foundational study of Brillouin flow that is applicable to both MILOs and RMs. Brillouin flow is also well investigated [40]–[69] and is generally regarded as the prevalent equilibrium state in crossed-field devices [32], [44], [52], [55], [57], [67], [68]. Our recent particle-in-cell simulations on these devices reliably show a profile consistent with Brillouin flow, albeit with some noise due to the finite particle nature of the simulation [66], [67]. The Brillouin flow profile has been used to derive the Hull-cutoff (HC) condition and the BH condition for magnetrons [8], [44], [46], [48], [57], [69]. It will also be used in this article to obtain, for the first time, the BH for a cylindrical MILO with an axial electron flow, which is the most common MILO configuration. Novel scaling laws, which shall be derived in this article, will elucidate the crucial parameters that control MILO performance according to the Brillouin flow model. Since the Brillouin flow is postulated to be the unperturbed flow, we assume that the electron spokes are drawn from it and that the electrons in the spokes convert their potential energy to coherent radiation, for both magnetrons and MILOs. *We must stress that the Brillouin flow is assumed to be the basic state for both MILOs and magnetrons treated in this article.* The amount of current carried within the Brillouin hub then represents the maximum current available to form electron spokes in both magnetrons, MILOs, and their hybrid.

There are difficulties in obtaining the relativistic Brillouin flow solutions, in general, and in obtaining the BH in MILOs and in cylindrical relativistic magnetrons, in particular.

A) The self-magnetic field due to the Brillouin flow electrons was considered very significant, and there is no simple, closed-form solution to quantify it, in general.

B) BH is a plot of gap voltage versus magnetic field. The importance of the self-magnetic field is unclear in this picture. While Lau *et al.* [69] solved this problem by using the gap voltage and the total magnetic flux and showed that the BH is very different between the Brillouin flow model and the widely used single-particle orbit model [70] for a cylindrical magnetron, they did not consider the cylindrical MILO.

C) In the Brillouin flow description of the smooth bore MILO, the anode current is different from the cathode current by the amount equal to the total electron current carried in the Brillouin hub [50], [51]. The use of gap voltage and diode impedance diminishes the role of
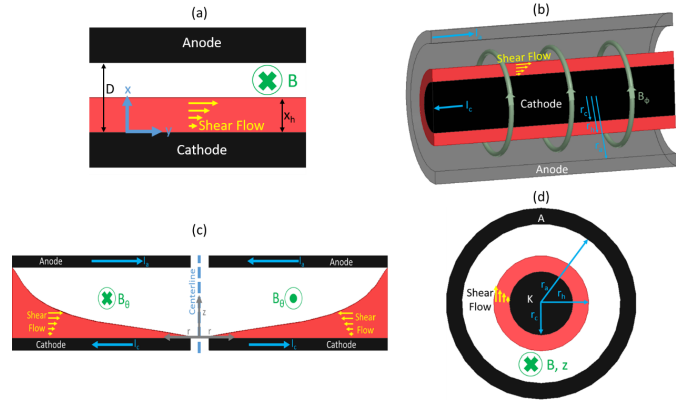

Fig. 1. Four (4) crossed-field diodes studied in this article, and their Brillouin flow profiles with electrons shown in red, flow velocity profiles shown by yellow arrows, and magnetic field shown in green. (a) Planar geometry modeling the magnetron, MILO, and their hybrid. (b) Cylindrical MILO with axial electron flow. (c) Cylindrical MITL with radial electron flow. (d) Cylindrical magnetron with azimuthal electron flow. Magnetic insulation may be provided by an external magnetic field, as in (d), or by wall currents, as in (b) and (c), or by an arbitrary mix of external magnetic field or wall currents, as in (a).

the electron current whose magnitude and profile are geometry-dependent and not readily available.

In a magnetron, the two external parameters commonly used to characterize the Brillouin flow are naturally the gap voltage and the magnetic field, because the magnetic field is provided by an external magnet. The dc current plays a secondary role. In fact, in the conventional magnetron model, the dc current is drawn only after oscillations have started [32], [35]. In MILO and magnetically insulated transmission line (MITL) [3], [4], it is natural to use the gap voltage and the current (or diode impedance) as the two major parameters. The magnetic field does not explicitly enter. Thus, as we struggle to find a general Brillouin flow solution that is applicable to all crossed-field geometries, including magnetrons, MILOs (and their hybrids), and MITLs, we must find another external parameter (other than the magnetic field or the current) in addition to the gap voltage (V_a). This second parameter is the vector potential, or the total magnetic flux (A_a) within the anode-cathode (AK) gap which, as we shall show, is equivalent to specifying the degree of magnetic insulation. Thus, for the entire Brillouin flow problem, regardless of the geometry or voltages, the two fundamental quantities are simply the scalar potential and the vector potential at the anode, assuming the values of both potentials equal to zero at the cathode. For both planar and cylindrical MILOs, the HC and BH conditions depend only on these two parameters and are independent of the geometry and of the mode of operation, in the manner shown in Fig. 2. Additionally, the closed-form explicit solution of the entire Brillouin flow may be obtained in terms of these two external parameters. This Brillouin flow solution is also independent of how the magnetic flux A_a is produced. Thus, it is applicable to the magnetron, MILO, and MITL geometries.

The generality of the above approach enables consideration of four representative cases, as shown in Fig. 1.

a) A planar magnetron whose magnetic field is provided by an external magnet, a planar MILO (or MITL)

whose magnetic field is exclusively generated by the wall currents (i.e., without an external magnetic field), or some combination of the two, which we call the magnetron–MILO hybrid.

  b) A cylindrical MILO (or MITL) whose magnetic field is generated by the axial wall currents on the anode and cathode, without any external magnetic field.

  c) A MITL in which there is no external magnetic field and magnetic insulation is provided by the radially converging current flows on the circular anode and cathode plates.

  d) A cylindrical magnetron in which the axial magnetic field is provided by an external magnet and the Brillouin flow is in the azimuthal direction.

The cases a) and b) have exact, closed-form solutions in all quantities of the Brillouin flow, and case c) has accurate approximate solutions over the main region of magnetic insulation. These three cases contain all of the new results stated in the Abstract; the useful scaling laws that led to these new results are derived in Appendix A. Case d) was solved in [69] and is only briefly summarized here for completeness. The main findings of this article are summarized below.

  1) In terms of V_a and A_a, we have found an explicit, analytic solution of the Brillouin flow for all geometries shown in Fig. 1, except the cylindrical magnetron with azimuthal flow [Fig. 1(d)] which required numerical computations. These explicit analytic solutions lead to the BH and HC conditions for the cylindrical MILO [Fig. 1(b)]. They are the same as those obtained from single-particle orbit model, as shown in Appendix B. The BH and HC thus obtained (Fig. 2) turn out to be also applicable to the planar magnetron and MILO, or some combination of the two, in which the total magnetic flux (A_a) is partially provided by an externally imposed magnetic field and partially provided by the wall currents as in a MILO.

  2) The explicit analytic solutions lead to scaling laws for various quantities of the Brillouin flow such as the Brillouin flow hub height, flow velocity at the top of the Brillouin flow, and the self-magnetic field that the Brillouin flow created. These scaling laws, derived in Appendix A, illuminate quantitatively the efficiency comparison between MILOs and magnetrons, based on the two parameters, V_a and A_a, once we assume similar mechanisms for spoke formation and for conversion of the potential energy to RF, for MILO, RM, and their hybrid.

  3) The self-magnetic field associated with the Brillouin flow is only a small fraction of that required for magnetic insulation whenever the total magnetic field exceeds 1.5 times the Hull magnetic field. The Brillouin hub height is a small fraction of the AK gap separation. These statements are independent of the gap voltage.

  4) The scaling laws show that MILO efficiency is limited to single digits, if we assume that the electron physics behind its operation is the same as a magnetron in this Brillouin flow model. MILO efficiency is even lower at nonrelativistic voltage, making a low-voltage
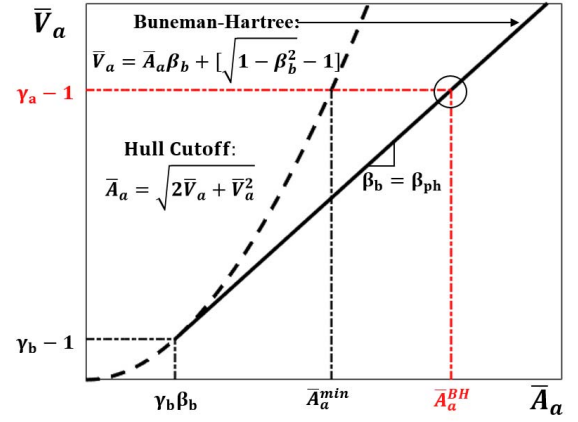

Fig. 2. BH and the HC condition in terms of the normalized gap voltage ($\bar{V}_a$) and normalized total magnetic flux ($\bar{A}_a$) according to the Brillouin flow model. These curves are applicable to the planar magnetron, planar MILO, their hybrid [Fig. 1(a)], and to the cylindrical MILO [Fig. 1(b)] regardless of its geometrical aspect ratio. Given ($\bar{V}_a, \bar{A}_a$), the circled point is the operating point that satisfies BH, that is, the phase velocity of the operating mode equals to the Brillouin flow velocity at the top of the electron hub. The point of tangency between the BH and HC curves is given in terms of β_b and $\gamma_b = 1/\sqrt{1 - \beta_b^2}$ defined in (2.34). Equation (2.28) gives $\bar{A}_a^{\min}$, which is the minimum value of $\bar{A}_a$ to achieve magnetic insulation at a given gap voltage. This graph is also valid for the three RF sources shown in Fig. 1(a), (b), and (d) according to the single-particle orbit model, if β_{ph} is taken to be the normalized phase speed at the anode of the operating mode in these three classes of devices.

MILO running at 50 kV very inefficient. However, a lower current MILO, running at 250 kV and 10 kA, is viable, which was demonstrated in our recent experiments [71], [72].

  5) For the radial MITL [Fig. 1(c)], the Brillouin flow profile is a function of radius. We derive the approximate Brillouin flow profile for the various radii at which magnetic insulation exists. We use the gap voltage and the anode current as the input parameters, after we relate them to V_a and A_a for each radius.

We treat the four configurations in Fig. 1(a)–(d), respectively, in Sections II–V. The planar geometry of Fig. 1 will be treated in detail in Section II, including the dominant scaling and useful formulas, many of which are used in Sections III–V. Each of these sections may be read independently. Additional issues are discussed in Section VI.

For all four geometries shown in Fig. 1, we will non-dimensionalize the governing equations using the speed of light c as the velocity scale, from which the following scales may be constructed. They are all universal constants

$$V_s = \text{voltage scale} = mc^2/e = 511 \text{ kV}$$

$$A_s = \text{vector potential scale} = mc/e \tag{1.1}$$

$$= 1.706 \times 10^{-3} \text{ T-m} \tag{1.2}$$

$$v_s = \text{velocity scale} = c = 3 \times 10^8 \text{ m/s} \tag{1.3}$$

$$I_s = \text{current scale} = mc/(e\mu_0) = 1.358 \text{ kA}. \tag{1.4}$$

Note that I_s equals 511 kV/377 Ω = 17 kA/(4π). Next, introduce the length scale, x_s, and further construct

the following scales:

$$E_s = \text{electric field scale} = V_s/x_s = mc^2/(ex_s)$$
$$= (5.11 \times 10^7 \text{ V/m}) * (1 \text{ cm}/x_s) \qquad (1.5)$$

$$B_s = \text{magnetic field scale} = A_s/x_s$$
$$= mc/(ex_s) = 0.1706\text{T} * (1 \text{ cm}/x_s) \qquad (1.6)$$

$$H_s = \text{magnetization scale} = B_s/\mu_0$$
$$= mc/(ex_s\mu_0)$$
$$= (1.358 \text{ kA/cm}) * (1 \text{ cm}/x_s) \qquad (1.7)$$

$$K_s = \text{surface current density scale} = H_s$$
$$= mc/(ex_s\mu_0)$$
$$= (1.358 \text{ kA/cm}) * (1 \text{ cm}/x_s) \qquad (1.8)$$

$$J_s = \text{current density scale} = I_s/x_s^2$$
$$= mc/(e\mu_0 x_s^2)$$
$$= (1.358 \text{ kA/cm}^2) * (1 \text{ cm}/x_s)^2 \qquad (1.9)$$

$$n_s = \text{number density scale} = \epsilon_0 E_s/(ex_s)$$
$$= \epsilon_0 mc^2/(e^2 x_s^2)$$
$$= (2.82 \times 10^{11}/\text{cm}^3) * (1 \text{ cm}/x_s)^2. \qquad (1.10)$$

All dimensionless variables are designated with a bar, after being divided by their respective scales. Thus

$$\bar{x} = x/x_s, \quad \bar{r} = r/x_s \qquad (1.11)$$
$$\bar{\phi} = \phi/V_s, \quad \bar{A} = A/A_s \qquad (1.12)$$
$$\bar{v} \equiv \beta = v/c, \quad \bar{I} = I/I_s \qquad (1.13)$$
$$\bar{E} = E/E_s, \quad \bar{B} = B/B_s \qquad (1.14)$$
$$\bar{H} = H/H_s, \quad \bar{K} = K/K_s \qquad (1.15)$$
$$\bar{J} = J/J_s, \quad \bar{n} = n/n_s. \qquad (1.16)$$

In Cartesian geometry [Fig. 1(a)], we set x_s equal to D, the gap spacing, and $\bar{x} = x/D$. The governing equations for the planar Brillouin flow, in dimensionless form, are given by (2.1)–(2.10). Their exact, closed-form solutions are derived in Section II. In the cylindrical MILO geometry with an axial Brillouin flow [Fig. 1(b)], we set x_s equal to r_a, the anode radius, and $\bar{x} = \bar{r} = r/r_a$. The governing equations for the Brillouin flow for cylindrical MILOs (and cylindrical MITLs) are given by (2.1), (2.2), (3.2), (3.3), and (2.5)–(2.10). The exact, closed-form solution to these equations, together with the BH condition, is derived in Section III. Note that in the normalized governing equations, (2.1)–(2.10), there are *only* two free parameters, the gap voltage and the total magnetic flux, V_a and A_a, and they enter only in the boundary conditions (2.8) and (2.9). The geometries for Fig. 1(c) and (d) will be similarly treated in Sections IV and V, where their solutions are outlined.

Since the use of vector potential is uncommon among experimentalists, a few words on their use are in order. Once the anode voltage V_a and the anode vector potential (or equivalently the total magnetic flux per unit length) A_a are specified, their normalized values $\bar{V}_a = V_a/V_s$ and $\bar{A}_a = A_a/A_s$ are immediately known using (1.1) and (1.2). The gap voltage gives the relativistic factors γ_a, β_a given in (2.27), as well as the quantity $\bar{A}_a^{\min}$ given in (2.28). We shall see that $\bar{A}_a^{\min}$ is the minimum normalized magnetic flux required for magnetic

insulation. Thus, the quantity $\bar{A}_a/\bar{A}_a^{\min}$ measures the degree of magnetic insulation. It is roughly equal to B/B_H because of result 3) summarized above, where B_H is the HC magnetic field. Thus, in place of (V_a, A_a), we may alternatively use V_a, and the degree of magnetic insulation $\bar{A}_a/\bar{A}_a^{\min}$, as the two fundamental, but more familiar parameters. Figs. 3–8 are presented this way.

II. PLANAR BRILLOUIN FLOW

For the planar geometry shown in Fig. 1(a), the cathode is located at $x = 0$ and the anode is located at $x = D$. The electrostatic field $E_x = -\partial\phi/\partial x$, and the magnetostatic field $B_z = \partial A_y/\partial x$, are given in terms of the scalar potential $\phi(x)$ and the vector potential $A_y(x)$, respectively. Without loss of generality, we set $\phi(0) = 0$ and $A_y(0) = 0$ on the cathode, and $\phi(D) = V_a > 0$ and $A_y(D) = A_a > 0$ on the anode. Hereafter, we assume that the AK voltage drop V_a and the total magnetic flux per unit length in y within the AK gap, A_a, are pre-specified, whether or not the gap is filled with space charge and space current, and whether or not this magnetic flux is provided by an external magnet (as in a planar magnetron), or by the wall currents on the anode and cathode (as in a planar MILO or planar MITL), or by some mixture of the two (as in a magnetron–MILO hybrid). Note that if this magnetic flux is provided only by an external dc magnetic field (B) that has been in existence for a long time, so that B has diffused into the anode and cathode surfaces, then $K_c = 0$ and $K_a = 0$, where K_c and K_a are, respectively, the surface current on both the metallic cathode and anode surfaces. If, in the other extreme, the total magnetic flux A_a is produced only by the surface currents K_c and K_a, without any externally imposed magnetic field, then $K_c = B_c/\mu_0$ and $K_a = B_a/\mu_0$, where B_c and B_a are, respectively, the magnetic fields adjacent to the metallic cathode and anode surfaces, whether or not the gap is filled with space charge and space current.

Thus, by specifying the total magnetic flux A_a within the gap, we leave it completely general without specifying how it is produced. In Section II-A, we construct the closed-form, explicit solutions for the Brillouin flow profile, including the spatial dependence in the space charge density, electron velocity profile, and the electric and magnetic field distributions within the gap. All of them depend only on the two input parameters, V_a and A_a. In Section II-B, we construct the BH and HC conditions from these Brillouin flow solutions. In Section II-C, we summarize the asymptotic formulas for deeply magnetically insulated diodes, which are derived in Appendix A. The scaling laws developed in Appendix A help clarify some confusion found in the literature. Much of the theory developed here will be applicable when we treat the other configurations shown in Fig. 1.

A. Brillouin Flow Solutions in a Planar Gap

For the Brillouin flow in the planar gap shown in Fig. 1(a), we use the AK gap spacing, D, as the length scale x_s. The normalized governing equations and the boundary conditions for the Brillouin flow are

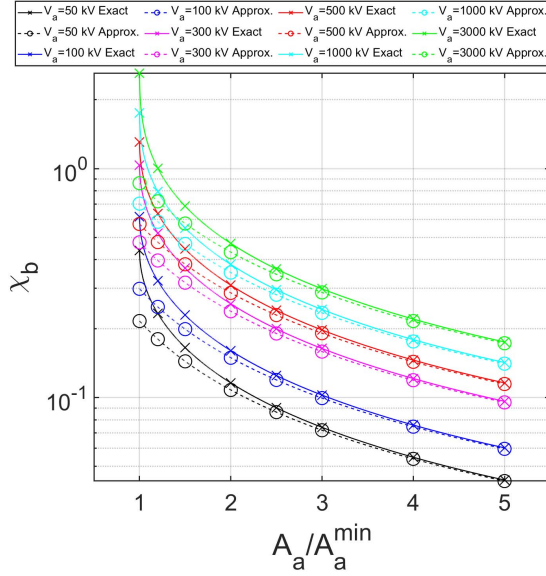$$\bar{E} = \partial\bar{\phi}/\partial\bar{x} \qquad (2.1)$$

Fig. 3. Parameter χ_b as a function of $\bar{A}_a/\bar{A}_a^{\min}$, the degree of magnetic insulation, at various gap voltages, obtained from the exact expressions (2.26). The dashed curves represent the asymptotic formula (2.39). The exact values and the errors in the asymptotic formula are tabulated in Table I. This graph, and Table I, are applicable to the three configurations shown in Fig. 1(a)–(c).

Fig. 4. Parameter κ as a function of $\bar{A}_a/\bar{A}_a^{\min}$, the degree of magnetic insulation, at various gap voltages, obtained from the exact expressions (2.29). The dashed curves represent the asymptotic formula (2.40). The exact values and the errors in the asymptotic formula are tabulated in Table II. This graph and Table II are applicable to the three configurations shown in Fig. 1(a)–(c).

TABLE I

χ_b VALUES FROM (2.26), THE ANALYTIC SOLUTION

$\dfrac{A_a}{A_a^{min}}$	$V_a =$ 50 kV	$V_a =$ 100 kV	$V_a =$ 200 kV	$V_a =$ 300 kV	$V_a =$ 400 kV	$V_a =$ 500 kV
1.1	0.2790	0.3880	0.5314	0.6316	0.7090	0.7718
1.2	0.2329	0.3232	0.4413	0.5229	0.5854	0.6358
1.5	0.1654	0.2291	0.3115	0.3680	0.4109	0.4451
2	0.1159	0.1603	0.2177	0.2567	0.2862	0.3096
2.5	0.0902	0.1248	0.1693	0.1995	0.2223	0.2404
3	0.0741	0.1025	0.1390	0.1638	0.1825	0.1973
4	0.0549	0.0759	0.1029	0.1212	0.1349	0.1459
5	0.0436	0.0603	0.0818	0.0963	0.1073	0.1159

TABLE II

κ VALUES FROM (2.29), THE ANALYTIC SOLUTION

$\dfrac{A_a}{A_a^{min}}$	$V_a =$ 50 kV	$V_a =$ 100 kV	$V_a =$ 200 kV	$V_a =$ 300 kV	$V_a =$ 400 kV	$V_a =$ 500 kV
1.1	0.4866	0.6884	0.9747	1.1964	1.3853	1.5541
1.2	0.5334	0.7580	1.0830	1.3404	1.5644	1.7682
1.5	0.6719	0.9619	1.3932	1.7459	2.0610	2.3537
2	0.9006	1.2957	1.8933	2.3913	2.8425	3.2665
2.5	1.1283	1.6267	2.3860	3.0233	3.6040	4.1520
3	1.3556	1.9566	2.8754	3.6496	4.3570	5.0259
4	1.8096	2.6146	3.8498	4.8943	5.8511	6.7576
5	2.2632	3.2716	4.8213	6.1339	7.3377	8.4792

PERCENT DIFFERENCE FROM THE EXACT VALUES EQ. (2.26) OF THE APPROXIMATE FORMULA (2.39)

$\dfrac{A_a}{A_a^{min}}$	$V_a =$ 50 kV	$V_a =$ 100 kV	$V_a =$ 200 kV	$V_a =$ 300 kV	$V_a =$ 400 kV	$V_a =$ 500 kV
1.1	29.63	30.05	30.79	31.43	32.00	32.49
1.2	22.71	23.03	23.60	24.08	24.51	24.88
1.5	12.93	13.11	13.43	13.70	13.94	14.14
2	6.80	6.90	7.07	7.21	7.33	7.44
2.5	4.24	4.30	4.40	4.49	4.57	4.63
3	2.90	2.94	3.02	3.08	3.13	3.17
4	1.61	1.63	1.67	1.71	1.74	1.76
5	1.03	1.04	1.07	1.09	1.10	1.12

PERCENT DIFFERENCE FROM THE EXACT VALUES EQ. (2.29) OF THE APPROXIMATE FORMULA (2.40)

$\dfrac{A_a}{A_a^{min}}$	$V_a =$ 50 kV	$V_a =$ 100 kV	$V_a =$ 200 kV	$V_a =$ 300 kV	$V_a =$ 400 kV	$V_a =$ 500 kV
1.1	2.42	4.75	9.18	13.31	17.19	20.83
1.2	1.93	3.77	7.20	10.33	13.21	15.86
1.5	1.15	2.22	4.16	5.88	7.42	8.80
2	0.61	1.18	2.20	3.08	3.85	4.53
2.5	0.39	0.74	1.37	1.91	2.38	2.79
3	0.26	0.51	0.94	1.30	1.62	1.90
4	0.15	0.28	0.52	0.72	0.90	1.05
5	0.09	0.18	0.33	0.46	0.57	0.67

$$\bar{B} = \partial \bar{A}/\partial \bar{x} \qquad (2.2)$$

$$\partial \bar{E}/\partial \bar{x} = \bar{n} \qquad (2.3)$$

$$\partial \bar{B}/\partial \bar{x} = \bar{n}\beta \qquad (2.4)$$

$$\bar{E} = \beta \bar{B} \qquad (2.5)$$

$$\bar{\phi} = \gamma - 1, \quad \gamma = \frac{1}{\sqrt{1 - \beta^2}} \qquad (2.6a,b)$$

$$\bar{A} = \gamma \beta \qquad (2.7)$$

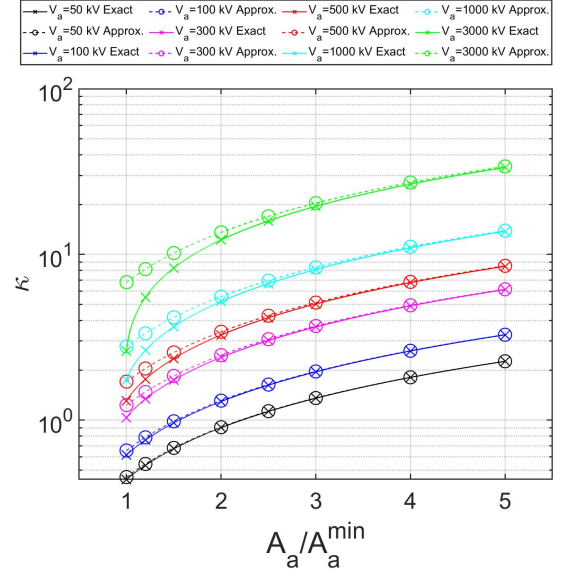$$\bar{\phi}(\text{cathode}) = 0, \quad \bar{\phi}(\text{anode}) = \bar{V}_a \qquad (2.8)$$

$$\bar{A}(\text{cathode}) = 0, \quad \bar{A}(\text{anode}) = \bar{A}_a \qquad (2.9)$$

$$\beta(\text{cathode}) = 0, \quad \bar{E}(\text{cathode}) = 0 \qquad (2.10a,b)$$

where, and in the remaining of this article, we have adopted the convention that the quantities $\bar{E}$, $\bar{B}$, $\bar{\phi}$, $\bar{A}$, $\bar{n}$, β, V_a, and A_a are all positive within the AK gap, which is $0 < \bar{x} < 1$ for the planar case. Equations (2.1) and (2.2) express the electric and magnetic field in terms of the scalar potential and vector potential, respectively. Equation (2.3) is the Poisson equation, (2.4) is Ampere's law, (2.5) states that all electrons move at the
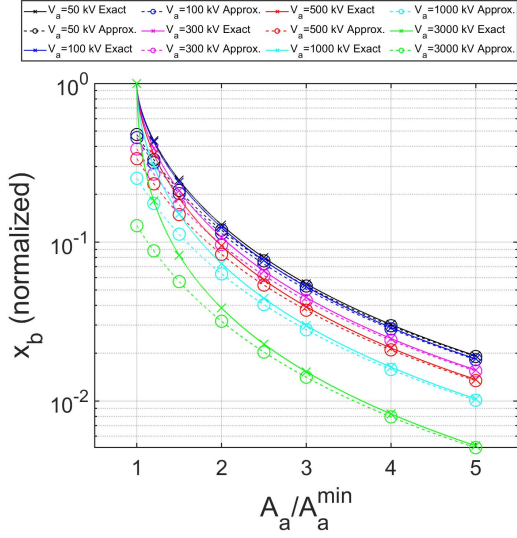
Fig. 5. Normalized Brillouin hub height, $\bar{x}_b$, for the planar diode [Fig. 1(a)] as a function of $\bar{A}_a/\bar{A}_a^{\min}$, the degree of magnetic insulation, at various gap voltages, obtained from the exact expressions (2.30). The dashed curves represent the asymptotic formula (2.41). Note that at fixed $\bar{A}_a/\bar{A}_a^{\min}$, the Brillouin hub height decreases as gap voltage increases, and for a very high-voltage MITL, (2.46) implies that the total electron current within the Brillouin hub approaches a constant, which is a small fraction of the wall current that provides magnetic insulation.
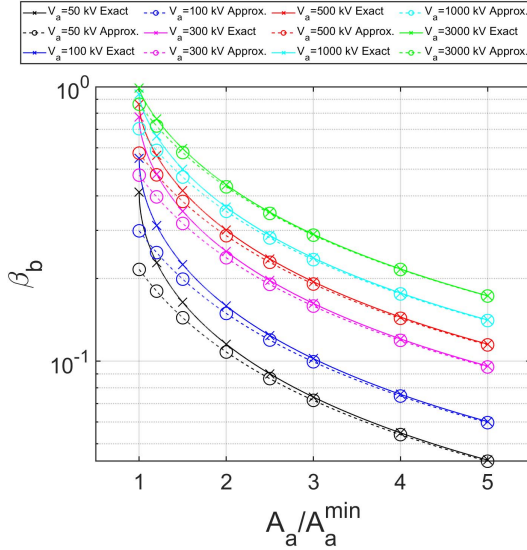

Fig. 6. Normalized electron flow velocity at the top of the Brillouin hub, β_b, for the planar diode [Fig. 1(a)] as a function of $\bar{A}_a/\bar{A}_a^{\min}$, the degree of magnetic insulation, at various gap voltages, obtained from the exact expression (2.34). The dashed curves represent the asymptotic formula (2.42).

local $E \times B$ drift velocity, (2.6) states conservation of energy for each electron, (2.7) states conservation of the canonical momentum in the y-direction, (2.8) and (2.9) specify the AK gap voltage and the total magnetic flux within the AK gap per unit length in y, and (2.10) states that the electron flow velocity and the electric field are both zero on the cathode surface, which are the major assumptions in the Brillouin flow solution. Equations (2.5)–(2.7) apply only within the Brillouin hub, outside which the left hand sides (LHSs) are the vacuum solutions. The vacuum field solutions are given by (2.20) and (2.21).
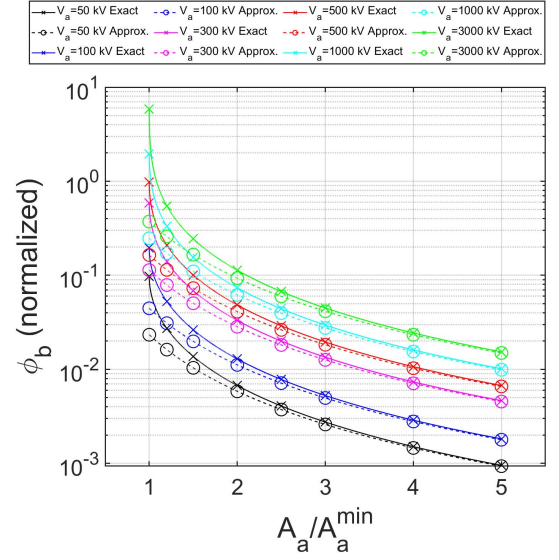

Fig. 7. Normalized electron kinetic energy (which is equal to the normalized potential energy in magnitude) at the top of the Brillouin hub, $\bar{\phi}_b$, for the planar diode [Fig. 1(a)] as a function of $\bar{A}_a/\bar{A}_a^{\min}$, the degree of magnetic insulation, at various gap voltages, obtained from the exact expression (2.14) with $\chi = \chi_b$. The dashed curves show the asymptotic formula (2.43).

The exact, closed-form analytic solutions to the nonlinear equations, (2.1)–(2.7), together with the boundary conditions (2.8)–(2.10), may be constructed following [45], [46], [48]. We first express all quantities within the Brillouin hub through the function

$$\chi = \chi(\bar{x}), \quad \chi(\bar{x}_c) = 0 \qquad (2.11\text{a,b})$$

where $\bar{x}_c$ is the value of $\bar{x}$ evaluated on the cathode surface [$\bar{x}_c = 0$ for Fig. 1(a)]. Specifically, we write [45], [46], [48], [69]

$$\beta = \tanh(\chi) \qquad (2.12)$$

so that the boundary condition (2.10a) is satisfied. With $\chi' \equiv \partial\chi(\bar{x})/\partial\bar{x}$, we obtain

$$\gamma = \cosh(\chi) \qquad (2.13)$$
$$\bar{\phi} = \cosh(\chi) - 1 \qquad (2.14)$$
$$\bar{A} = \sinh(\chi) \qquad (2.15)$$
$$\bar{E} = \chi'\sinh(\chi) \qquad (2.16)$$
$$\bar{B} = \chi'\cosh(\chi) \qquad (2.17)$$
$$\bar{n} = \partial\left[\chi'\sinh(\chi)\right]/\partial\bar{x} \qquad (2.18)$$

which follow, respectively, from (2.6b), (2.6a), (2.7), (2.1), (2.2), and (2.3). We next substitute (2.17), (2.18), and (2.12) into (2.4), which may be shown to reduce to $(\partial^2\chi(\bar{x})/\partial\bar{x}^2) = 0$, yielding

$$\chi(\bar{x}) = \kappa\bar{x} \qquad (2.19)$$

for some constant κ, upon using the boundary condition (2.11b). This constant κ, which equals to χ' by (2.19), and the normalized Brillouin hub height, $\bar{x}_b$, will be determined next in terms of the AK gap voltage ($\bar{V}_a$) and the magnetic flux ($\bar{A}_a$). Note that once κ and $\bar{x}_b$ are determined, the Brillouin flow profile may be obtained from (2.12)–(2.19), and the BH
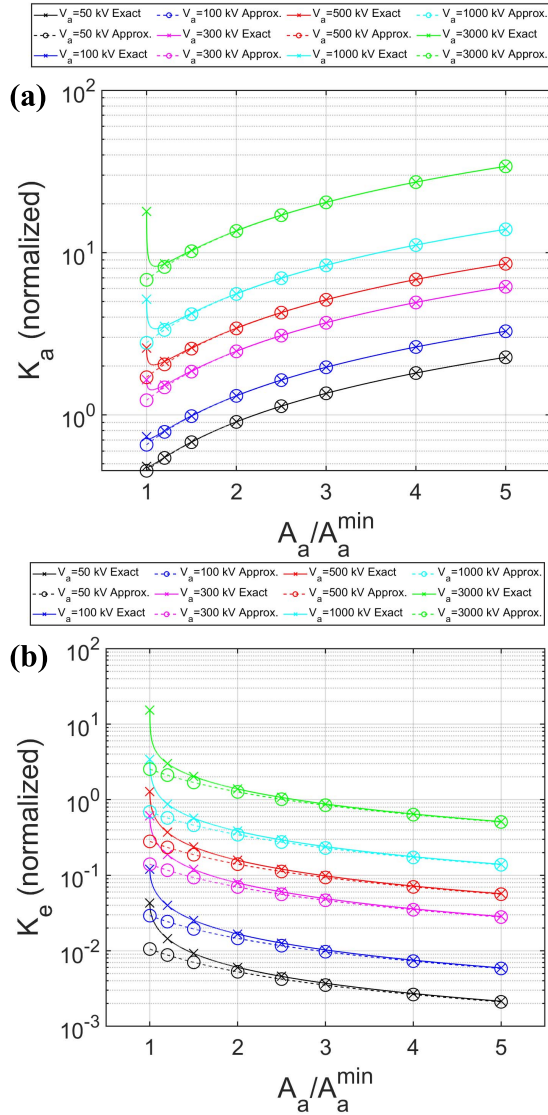
Fig. 8. (a) Normalized anode wall current $\bar{K}_a$ and (b) normalized electron current carried within the Brillouin hub $\bar{K}_e$, in a planar MILO or MITL [Fig. 1(a)] as a function of $\bar{A}_a/\bar{A}_a^{\min}$, the degree of magnetic insulation, at various gap voltages, obtained from the exact expressions $\bar{K}_a = \kappa\cosh(\chi_b)$ and $\bar{K}_e = \kappa[\cosh(\chi_b) - 1]$. The dashed curves represent the asymptotic formulas (2.44) and (2.45). Note that $\bar{K}_e \ll \bar{K}_a$ by at least one order of magnitude whenever $\bar{A}_a/\bar{A}_a^{\min} > 1.5$, regardless of the anode voltage, implying that the electron current within the Brillouin hub always contributes little to magnetic insulation.

condition and the HC conditions immediately follow, whether the device is a planar MILO or planar relativistic magnetron, or some mixture of the two. These BH and HC conditions are shown in Fig. 2.

In the vacuum region, $\bar{x}_b < \bar{x} < 1$, both $\bar{\phi}$ and $\bar{A}$ are linear functions of $\bar{x}$:

$$\bar{\phi}(\bar{x}) = \bar{\phi}_b + \bar{E}_b(\bar{x} - \bar{x}_b) \quad (2.20)$$

$$\bar{A}(\bar{x}) = \bar{A}_b + \bar{B}_b(\bar{x} - \bar{x}_b) \quad (2.21)$$

where, and hereafter, the subscript "b" denotes the value at the top of the Brillouin hub, that is, at $\bar{x} = \bar{x}_b$ [Fig. 1(a)]. Evaluating (2.20) and (2.21) at the anode, $\bar{x} = 1$,

we obtain [46]

$$\bar{V}_a = \cosh(\chi_b) - 1 + \sinh(\chi_b) \times \kappa(1 - \bar{x}_b) \quad (2.22)$$

$$\bar{A}_a = \sinh(\chi_b) + \cosh(\chi_b) \times \kappa(1 - \bar{x}_b) \quad (2.23)$$

where we have used (2.14)–(2.17) to evaluate the corresponding quantities at the top of the Brillouin hub, $\bar{x} = \bar{x}_b$, and

$$\chi_b = \kappa \bar{x}_b \quad (2.24)$$

Equations (2.22) and (2.23) are two equations in two unknowns, χ_b and κ (after recognizing the factor $\kappa(1 - \bar{x}_b) = (\kappa - \chi_b)$ in these two equations), which can be solved in terms of $\bar{V}_a$ and $\bar{A}_a$. By eliminating the factor $[\kappa(1 - \bar{x}_b)]$ from (2.22) to (2.23), the quantity χ_b can be determined in terms of $\bar{V}_a$ and $\bar{A}_a$ from the following:

$$\bar{A}_a - \sinh(\chi_b) = [\bar{V}_a - (\cosh(\chi_b) - 1)]\coth(\chi_b). \quad (2.25)$$

We argue in Section II-B that, in terms of $\bar{V}_a$ and $\bar{A}_a$, the closed-form solution of χ_b to (2.25) may be written explicitly

$$\chi_b = \tanh^{-1}\left[\frac{\gamma_a\bar{A}_a - \sqrt{\bar{A}_a^2 - (\bar{A}_a^{\min})^2}}{\bar{A}_a^2 + 1}\right] \quad (2.26)$$

where

$$\gamma_a = \bar{V}_a + 1 \equiv 1/\sqrt{1 - \beta_a^2} \quad (2.27)$$

$$\bar{A}_a^{\min} = \gamma_a\beta_a. \quad (2.28)$$

As we shall see, $\bar{A}_a^{\min}$ is the minimum value of the normalized magnetic flux required to achieve magnetic insulation. It is important to note that $\bar{A}_a^{\min}$ depends only on the gap voltage and is independent of the geometry and that the ratio $\bar{A}_a/\bar{A}_a^{\min}$ then represents the degree of magnetic insulation. Appendix C proves directly that (2.26) is a solution to (2.25).

In terms of χ_b, the solution of κ may be obtained from (2.22), upon using (2.24)

$$\kappa = \frac{1}{\sinh(\chi_b)}[\bar{V}_a - (\cosh(\chi_b) - 1) + \chi_b\sinh(\chi_b)]. \quad (2.29)$$

The normalized hub height is given by (2.24)

$$\bar{x}_b = \chi_b/\kappa \quad (2.30)$$

in which χ_b and κ are given explicitly by (2.26) and (2.29) in terms of $\bar{V}_a$ and $\bar{A}_a$. The entire Brillouin flow profiles may then be obtained from (2.19), and (2.12)–(2.18), and the vacuum field solutions by (2.20) and (2.21). All quantities at the cathode, at the top of the Brillouin hub, and at the anode may be obtained by setting, respectively, the values of $\bar{x}$ equal to 0, $\bar{x}_b$, and 1 in these equations. Figs. 3–8 show the Brillouin flow parameters as a function of $\bar{A}_a/\bar{A}_a^{\min}$, the degree of magnetic insulation, at various values of $\bar{V}_a$. The two most important parameters, χ_b and κ, are plotted in Figs. 3 and 4. Their numerical values are listed in Tables I and II, including the errors in the approximate expressions using the scaling laws (2.39) and (2.40). We shall describe these graphs shortly in Section II-C, after we discuss in Section II-B the HC and BH conditions that led to (2.26)–(2.28).

B. HC and BH Condition in a Planar Gap

Given the gap voltage $\bar{V}_a$, the HC condition specifies the minimum value of the magnetic flux, $\bar{A}_a^{\min}$, that is required to prevent the Brillouin hub from reaching the anode. At this minimum value of magnetic flux, an electron at the top of the Brillouin hub barely touches the anode; its relativistic mass factor, γ_a, is then given by (2.27) by virtue of (2.6a), with the associated normalized flow velocity, β_a, also given by (2.27). This minimum magnetic flux, $\bar{A}_a^{\min} = \gamma_a \beta_a$, then follows from (2.7), and was displayed as (2.28). The HC condition, $\bar{A}_a = \bar{A}_a^{\min}$, may be rewritten in the more familiar form upon using (2.27)

$$\bar{A}_a = \sqrt{\bar{V}_a^2 + 2\bar{V}_a} \qquad (2.31)$$

which is plotted in Fig. 2.

Under the condition of magnetic insulation, $\bar{A}_a > \bar{A}_a^{\min}$, the BH condition stipulates that the phase velocity of the circuit wave, v_{ph}, evaluated at the top of the Brillouin hub, is equal to the Brillouin flow velocity there, that is,

$$\beta_{\text{ph}} = \frac{v_{\text{ph}}}{c} = \beta_b \equiv \beta(\bar{x}_b). \qquad (2.32)$$

Since the BH according to this Brillouin flow formulation has been proved to be identical to the BH according to the single-particle orbit model in a *planar* crossed-field gap [45], [46], [48], [69], we can immediately write down this BH as

$$\bar{V}_a = \bar{A}_a \beta_b + \left[\sqrt{1 - \beta_b^2} - 1 \right]. \qquad (2.33)$$

The BH condition (2.33) is shown in Fig. 2 as the straight line with a slope β_b. Equation (2.33) may be solved for β_b in terms of $\bar{V}_a$ and $\bar{A}_a$, yielding

$$\beta_b = \frac{\gamma_a \bar{A}_a - \sqrt{\bar{A}_a^2 - \left(\bar{A}_a^{\min}\right)^2}}{\bar{A}_a^2 + 1} = \tanh(\chi_b) \qquad (2.34)$$

where the last equality sign follows (2.12). The negative sign in front of the square root in (2.34) is chosen to ensure that $\beta_b < \beta_a$. Note that (2.34) is identical to (2.26). The BH, (2.33), is tangent to the HC condition, (2.31), in Fig. 2, and the point of tangency is given in terms of β_b and $\gamma_b = 1/(1 - \beta_b^2)^{1/2}$. We have also checked that the numerical values of χ_b (cf. Table I) obtained from (2.26) are the same as those obtained by the numerical solution of (2.25). Once more, it was previously shown [69] that the BH and HC relation given in Fig. 2, obtained from the Brillouin flow formulation, are identical to those obtained from single-particle model [70] for this planar geometry [Fig. 1(a)].

C. Properties of the Brillouin Flow and Scaling Laws

The ratio, $\bar{A}_a/\bar{A}_a^{\min}$, represents the degree of magnetic insulation. It is roughly equal to the ratio B/B_H, where B_H is the HC magnetic field. We say "roughly equal to" because the HC magnetic field is not well defined if the magnetic field is spatially nonuniform. These two ratios are equal if the magnetic flux is associated with the (spatially uniform) *vacuum* magnetic field, B, at a given AK gap voltage V_a. The solid curves in Figs. 3 and 4 show χ_b and κ, respectively, as a function of $\bar{A}_a/\bar{A}_a^{\min}$ at various gap voltages computed from

(2.26) and (2.29). The dashed curves in Figs. 3 and 4 show the asymptotic formulas, (2.39) and (2.40), under the assumption of deep magnetic insulation, $\bar{A}_a/\bar{A}_a^{\min} \gg 1$. We note that all curves for the exact values of χ_b in Fig. 3 have a negative infinite slope as $\bar{A}_a/\bar{A}_a^{\min} \to 1$, a property we shall prove in Appendix A, where we discuss this notable property as the diode is about to lose magnetic insulation. The normalized hub height, $\bar{x}_b$, given by (2.30), is plotted by the solid lines in Fig. 5, which shows that $\bar{x}_b < 0.15$ whenever $\bar{A}_a/\bar{A}_a^{\min} > 2$. The very small value of the Brillouin hub height compared with the AK gap spacing, at higher values of $\bar{A}_a/\bar{A}_a^{\min}$, means that the Brillouin flow itself may be treated in the Cartesian geometry to the lowest order, even for a cylindrical Brillouin flow. At a given degree of magnetic insulation, that is, at a fixed value of $\bar{A}_a/\bar{A}_a^{\min}$, Fig. 5 shows that the Brillouin hub height *decreases* as the AK gap voltage *increases*, which is unexpected intuitively. *This implies that in a high-voltage MITL that is deeply magnetically insulated, the Brillouin hub height is extremely thin and it lies very close to the cathode surface.* Its Brillouin flow carries only a small, but finite fraction of the wall current that is required to achieve this degree of magnetic insulation, as implied by the scaling law (2.46). The normalized electron flow velocity at the top of the Brillouin hub, $\beta_b = \tanh(\chi_b)$, is shown in Fig. 6 (solid lines). For $V_a < 250$ kV and $\bar{A}_a/\bar{A}_a^{\min} > 2$, which largely covers the operating regimes of commercial magnetrons, we find $\beta_b < 0.23$, corresponding to a kinetic energy of less than 15 kV. Fig. 7 shows the kinetic energy of the electrons at the top of the Brillouin hub. This kinetic energy also equals to the value of its electrostatic potential energy (in magnitude) at the top of the Brillouin hub by (2.6a).

All other field quantities at the cathode [anode] may be obtained from $\bar{\phi}$ and $\bar{A}$ as given by (2.14) and (2.15) [(2.20) and (2.21)] evaluated at $\bar{x} = 0$ [$\bar{x} = 1$]. In particular, the magnetic field adjacent to the anode, and to the cathode, is given by, respectively,

$$\bar{B}_a = \bar{B}_b = \kappa \cosh(\chi_b) \qquad (2.35)$$
$$\bar{B}_c = \kappa. \qquad (2.36)$$

If the magnetic flux is solely provided by the anode current (I_a) and the cathode current (I_c), as in the case of a planar MILO and MITL, these two currents are proportional to $\bar{B}_a$ and $\bar{B}_c$. The difference between I_a and I_c is the total current I_e that is carried by the electrons within the Brillouin hub, that is,

$$I_e = I_a - I_c \qquad (2.37)$$

where we have again adopted the conventions that all I's are positive. We thus arrive at the following ratios between the three currents:

$$I_a : I_c : I_e = \cosh(\chi_b) : 1 : [\cosh(\chi_b) - 1]$$
$$= (1 + \bar{\phi}_b) : 1 : \bar{\phi}_b. \qquad (2.38)$$

The last equality follows from (2.14). Fig. 8(a) shows the normalized anode current density $\bar{K}_a = \bar{B}_a = \kappa \cosh(\chi_b)$ in a planar MILO. The normalized cathode current density is $\bar{K}_c = \bar{B}_c = \kappa$. Their difference gives the normalized electron current carried within the Brillouin hub $\bar{K}_e = \bar{K}_a - \bar{K}_c$,

which is plotted in Fig. 8(b). Comparing Fig. 8(a) with (b), we see that in dimensional form, $K_e = I_e/W$ is much less than $K_a = I_a/W$ typically, where W is the width of the MILO out of the plane of this article in Fig. 1(a). This means that in a magnetically insulated diode, the self-magnetic field generated by the electron current residing within the Brillouin hub contributes little toward magnetic insulation. This is true, in general, whether the magnetic insulation is exclusively provided by the wall currents (I_a and I_c), as in a MILO, or exclusively provided by an external magnetic field, as in a magnetron, or by a combination of the two, as in their hybrid. Thus, it is misleading to state that the insulating magnetic field in a MILO is provided by the electron flow within the insulating gap. This is also the reason behind our assertion that $\bar{A}_a/\bar{A}_a^{\min}$ is roughly equal to the ratio B/B_H.

Finally, we note that in Fig. 8(a), the horizontal line $\bar{K}_a = 10$ (not shown) would intersect the solid green curve at two points. That is, the green curve, corresponding to $V_a = 3000$ kV, has a V-shape near $\bar{A}_a/\bar{A}_a^{\min} \cong 1$. In Appendix A, we show that all curves of $\bar{K}_a$ in Fig. 8(a) are of a V-shape very close to the HC, regardless of the anode voltage V_a. At the minimum of this V-shape curve, the anode current required to achieve magnetic insulation at this point ($\bar{A}_a/\bar{A}_a^{\min} > 1$) is *lower* than that required to achieve HC ($\bar{A}_a/\bar{A}_a^{\min} = 1$). This V-shape curve is an unexpected feature which is explored further in Appendix A. It affects our treatment of the radial MITL in Section V in the region where $\bar{A}_a/\bar{A}_a^{\min} \cong 1$. Finally, we remark here that the current ratios given in (2.38) holds for *all* geometries in Fig. 1(a)–(c) whenever the insulating magnetic field is solely provided by the wall currents I_a and I_c, (i.e., no external magnetic field).

To get an understanding of the scaling properties, we present the approximate formulas for the various Brillouin flow quantities in terms of $\bar{V}_a$ and $\bar{A}_a$, under the condition of deep magnetic insulation, $\bar{A}_a/\bar{A}_a^{\min} \gg 1$

$$\chi_b \approx \bar{V}_a/\bar{A}_a \tag{2.39}$$
$$\kappa \approx \bar{A}_a \tag{2.40}$$
$$\bar{x}_b \approx \bar{V}_a/\bar{A}_a^2 \tag{2.41}$$
$$\beta_b \approx \bar{V}_a/\bar{A}_a \tag{2.42}$$
$$\bar{\phi}_b \approx \frac{\left(\bar{V}_a/\bar{A}_a\right)^2}{2} \tag{2.43}$$
$$\bar{K}_a = \bar{B}_a = \bar{B}_b \approx \bar{A}_a \tag{2.44}$$
$$\bar{K}_e \approx \bar{V}_a^2/\left(2\bar{A}_a\right) \tag{2.45}$$
$$I_a : I_c : I_e \approx 1 : 1 : \frac{\left(\bar{V}_a/\bar{A}_a\right)^2}{2}. \tag{2.46}$$

These approximate solutions, (2.39)–(2.45), are displayed as dotted lines in Figs. 3–8. They are derived in Appendix A under the assumption of large $\bar{A}_a/\bar{A}_a^{\min}$. As shown in Figs. 3–8, these approximate formulas are fairly accurate for $\bar{A}_a/\bar{A}_a^{\min} = 2$ and become very accurate for $\bar{A}_a/\bar{A}_a^{\min} > 3$, corroborating the notion that the number three (3) is a sufficiently large dimensionless expansion parameter for an accurate asymptotic analysis. The relative errors in the approximate formulas, (2.39) and (2.40), are presented in Tables I and II. Appendix A also describes in some details the Brillouin

flow properties very close to HC, $\bar{A}_a/\bar{A}_a^{\min} \to 1$, a topic insufficiently addressed in the literature. The scaling laws, (2.39)–(2.46), shed some new light on the viability of building a low current MILO, or a low voltage MILO. These will be considered in Section III, where we treat the cylindrical MILO geometry [Fig. 1(b)].

III. CYLINDRICAL BRILLOUIN FLOW IN AXIAL DIRECTION

We now turn to the Brillouin flow for the cylindrical MILO geometry, as shown in Fig. 1(b), where the flow is in the z-direction and its Brillouin hub extends from the cathode radius r_c to the hub's outer edge at radius r_b. The anode is at radius r_a and is held at a gap voltage V_a with respect to the cathode. The electric field E is in the radial direction, the magnetic field is in the azimuthal direction, and the vector potential is in the z-direction. The total magnetic flux within the AK gap per unit length in z is A_a. As in the planar case treated in Section II, we will determine the closed-form, explicit Brillouin flow solution in terms of $\bar{V}_a$ and $\bar{A}_a$, the normalized gap voltage and total magnetic flux defined in (2.8) and (2.9). Section III-A gives the explicit, closed-form Brillouin flow profile solutions. Section III-B gives the HC and BH conditions for the cylindrical MILO geometry according to the Brillouin flow model (which will be shown to be the same as the single-particle cycloidal orbit model in Appendix B). Section III-C considers a few examples, including the high current MILO, and considerations for the viability of a moderate current MILO, a magnetron–MILO hybrid, and a low-voltage MILO.

We should note at the outset that, if we assume that the electron–circuit interaction is the same between a MILO and a magnetron, MILO would possess a very low efficiency, simply because of the very low electron current in the Brillouin flow (from which the RF-generating spoke current is drawn) compared with the wall currents that are needed to provide magnetic insulation for the MILO. This has been shown quantitatively in Fig. 8(a) and (b) and in the scaling law (2.46).

A. Cylindrical Brillouin Flow in the Axial Directions

For the cylindrical geometry [Fig. 1(b)], we use the anode radius, r_a, as the length scale. Thus, we write, for the cylindrical geometry [cf. (1.11)]

$$\bar{r} = r/r_a \equiv \bar{x} \tag{3.1}$$

where we again use $\bar{x}$ to denote the normalized radius so that many of the formulas in Section II can be used here. For example, (2.1), (2.2), and (2.5)–(2.17) are all valid for the cylindrical axial Brillouin flow studied here, together with their physical meanings, and the convention that all quantities ($\bar{E}, \bar{B}, \bar{\phi}, \bar{A}, \bar{n}, \beta, V_a, A_a$) are nonnegative. The Poisson equation (2.3) and Ampere's law (2.4) are now modified to read, respectively,

$$\frac{1}{\bar{r}} \frac{\partial}{\partial \bar{r}} \left(\bar{r}\bar{E}\right) = \bar{n} \tag{3.2}$$
$$\frac{1}{\bar{r}} \frac{\partial}{\partial \bar{r}} \left(\bar{r}\bar{B}\right) = \bar{n}\beta. \tag{3.3}$$

We next substitute (2.16) and (2.17) into (3.2) and (3.3). Equation (3.3) then reduces to the following equation for $\chi(\bar{r}) = \chi(\bar{x})$:

$$\frac{1}{\bar{r}}\frac{\partial}{\partial \bar{r}}\left(\bar{r}\frac{\partial \chi}{\partial \bar{r}}\right) = 0. \qquad (3.4)$$

The solution to (3.4), subject to the boundary condition (2.11b), which now reads $\chi(\bar{r}_c) = 0$, is given by

$$\chi(\bar{r}) = \bar{\kappa}\ln(\bar{r}/\bar{r}_c), \quad \chi' = \bar{\kappa}/\bar{r} \qquad (3.5)$$

for some constant $\bar{\kappa}$. Analogous to (2.20) and (2.21), the field solutions in the vacuum region read, $(\bar{r}_b < \bar{r} < 1)$:

$$\bar{\phi}(\bar{r}) = \bar{\phi}_b + \bar{E}_b\bar{r}_b\ln(\bar{r}/\bar{r}_b) \qquad (3.6)$$
$$\bar{A}(\bar{r}) = \bar{A}_b + \bar{B}_b\bar{r}_b\ln(\bar{r}/\bar{r}_b) \qquad (3.7)$$

where both $\bar{E}(\bar{r}) = \partial\bar{\phi}(\bar{r})/\partial\bar{r}$ and $\bar{B}(\bar{r}) = \partial\bar{A}(\bar{r})/\partial\bar{r}$ have $1/\bar{r}$ dependence. Equations (2.22) and (2.23) are modified to read

$$\bar{V}_a = \cosh(\chi_b) - 1 + \sinh(\chi_b) \times \bar{\kappa}\ln(1/\bar{r}_b) \qquad (3.8)$$
$$\bar{A}_a = \sinh(\chi_b) + \cosh(\chi_b) \times \bar{\kappa}\ln(1/\bar{r}_b). \qquad (3.9)$$

Upon eliminating the common factor, $\bar{\kappa}\ln(1/\bar{r}_b)$, in (3.8) and (3.9), we obtain the same transcendental equation (2.25) for χ_b whose analytic solution is given by (2.26) in terms of $\bar{V}_a$ and $\bar{A}_a$, copied here for convenience

$$\chi_b = \tanh^{-1}\left[\frac{\gamma_a\bar{A}_a - \sqrt{\bar{A}_a^2 - \left(\bar{A}_a^{\min}\right)^2}}{\bar{A}_a^2 + 1}\right] \qquad (3.10)$$

$$\gamma_a = \bar{V}_a + 1 \equiv 1/\sqrt{1 - \beta_a^2} \qquad (3.11)$$
$$\bar{A}_a^{\min} = \gamma_a\beta_a. \qquad (3.12)$$

To calculate $\bar{\kappa}$ and $\bar{r}_b$, we first evaluate (3.5) at $\bar{r} = \bar{r}_b$ to yield

$$\bar{\kappa}\ln(\bar{r}_b) = \bar{\kappa}\ln(\bar{r}_c) + \chi_b. \qquad (3.13)$$

Using (3.13) in (3.8), we obtain

$$\bar{\kappa} = \frac{1}{\ln(1/\bar{r}_c)}\left[\chi_b + \frac{\bar{V}_a - (\cosh\chi_b - 1)}{\sinh\chi_b}\right] \qquad (3.14)$$

which may also be written as

$$\bar{\kappa} = \kappa/\ln(1/\bar{r}_c) \qquad (3.14a)$$

where κ is the same as (2.29) which was studied in great detail in Section II, with values tabulated in Table II. Equation (3.13) yields

$$\bar{r}_b = \bar{r}_c e^{\chi_b/\bar{\kappa}}. \qquad (3.15)$$

Note that (3.14) and (3.15) give $\bar{\kappa}$ and $\bar{r}_b$ as explicit functions of $\bar{V}_a$ and $\bar{A}_a$ by virtue of (3.10). We now have the closed-form, analytic solution of the axial Brillouin flow profile given by (2.12)–(2.17), in which χ is given by (3.5). The vacuum fields exterior to the Brillouin hub are given by (3.6) and (3.7).

Since χ_b given in (2.26) is the same for cylindrical MILO (3.10) and for planar MILO, for a given set of $\bar{V}_a$ and $\bar{A}_a$, we may use Fig. 3 and the tabulated values in Table I. The values of $(\beta_b, \gamma_b, \bar{\phi}_b, \bar{A}_b)$ are also given by (2.12)–(2.15), so is
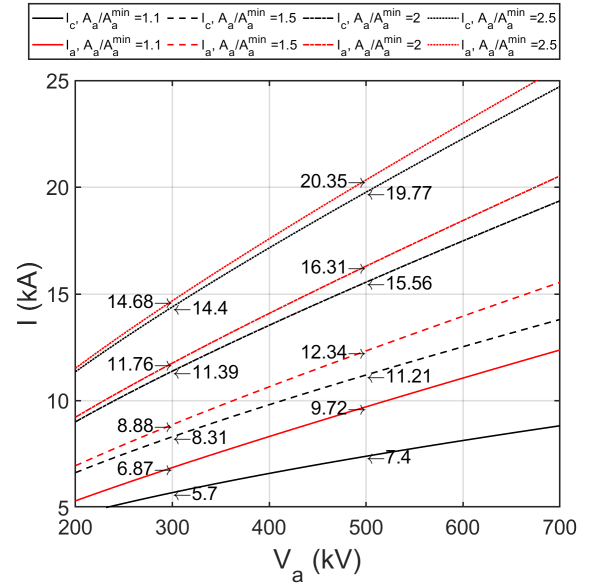

Fig. 9. Anode current I_a and the cathode current I_c as a function of gap voltage V_a, at various $\bar{A}_a/\bar{A}_a^{\min}$ in a cylindrical MILO [Fig. 1(b)] of aspect ratio $r_a/r_c = 6$. The values of I_a and I_c are specified in the graph for V_a at 300 and 500 kV. In each pair, the top number (in kA) denotes I_a and the bottom number denotes I_c, their difference denotes I_e, the total electron current carried within the Brillouin hub.

the ratio given by (2.38) between I_a, I_c, and I_e, regardless of the aspect ratio $\bar{r}_c$ or gap spacing in the cylindrical geometry. For the cylindrical MILO

$$\frac{I_c}{I_s} = \frac{2\pi r_c H_c}{I_s} = 2\pi\bar{r}_c\bar{H}_c = 2\pi\bar{\kappa} \qquad (3.16)$$

where we have used Ampere's law for the cathode current I_c, the scaling parameters I_s, H_s in (1.4) and (1.7), and (2.17) and (3.5) for the magnetic field on the cathode surface ($\chi = 0$). Since $I_s = 1.358$ kA by (1.4), we obtain from (3.16) and (2.38) the following expressions for the cathode, anode, and electron currents on a cylindrical MILO [Fig. 1(b)]:

$$I_c = (8.53 \text{ kA})\bar{\kappa}, \quad I_a = I_c\cosh(\chi_b)$$
$$I_e = I_a - I_c. \qquad (3.17)$$

Note that the ratio between I_a, I_c, and I_e is still given by (2.38), and this ratio depends only on $\bar{V}_a$ and $\bar{A}_a$ and is independent of the MILO radii r_a and r_c.

Fig. 9 plots the values of I_a and I_c as a function of V_a at various values of $\bar{A}_a/\bar{A}_a^{\min}$ according to (3.17), assuming the aspect ratio $1/\bar{r}_c = r_a/r_c = 6$. The total current carried by the electrons within the Brillouin hub equals to $(I_a - I_c)$. For a moderate-current MILO driven by a MELBA-like accelerator [9], we set $V_a = 300$ kV, and assume $\bar{A}_a/\bar{A}_a^{\min} = 1.5$, $r_c = 1$ cm, and $r_a = 6$ cm, then Fig. 9 gives $I_a = 8.88$ kA, $I_c = 8.31$ kA, and $I_e = I_a - I_c = 0.57$ kA is the electron current carried in the Brillouin hub, whose hub radius is at $r_b = 1.459$ cm according to (3.15). This example, and others, together with a discussion of MILO scaling, will be further examined in Section III-C.

B. HC and BH Conditions for a MILO With Cylindrical Axial Brillouin Flow

In the Brillouin flow picture, the HC condition is derived by requiring that the Brillouin hub barely touches the anode, that is, $\bar{r}_b = \bar{r}_a = 1$, whence $\gamma_b = \gamma_a = \bar{V}_a + 1 = \cosh(\chi_b)$. Use these expressions in (3.9) to yield

$$\bar{A}_a = \sinh(\chi_b) = \sqrt{\bar{V}_a^2 + 2\bar{V}_a} \qquad (3.18)$$

which was shown in Fig. 2. In Appendix B, we show that the same result is obtained from the single-particle orbit model for the cylindrical MILO. This is also the same HC condition (2.31) for planar MILO and planar magnetron, as shown in Fig. 2.

For BH, we note that the square bracket in (3.10) is the normalized electron flow speed, β_b, at the top of the Brillouin hub [cf. (2.12)]. It is also equal to the normalized phase velocity, β_{ph}, of the MILO operating mode according to BH in the Brillouin flow description. Since this β_b satisfies (2.33), which was already plotted in Fig. 2, (2.33) becomes BH by replacing β_b with β_{ph}

$$\bar{V}_a = \bar{A}_a\beta_{ph} + \left[\sqrt{1 - \beta_{ph}^2} - 1\right]. \qquad (3.19)$$

Appendix B shows that the single-particle orbit model also yields the same BH condition, (3.19), for the cylindrical MILO shown in Fig. 1(b). An analogous form was given in [13, Eq. (6)], but it is different from (3.19).

C. Scaling Laws and Examples

In this section, we establish the simple scaling laws for cylindrical MILO, once more assuming good magnetic insulation, $\bar{A}_a/\bar{A}_a^{min} \gg 1$. Some examples will be considered, including: 1) a high-current MILO; 2) a moderate-current MILO and a MILO–magnetron hybrid; and 3) a low-voltage MILO. Given $\bar{V}_a$ and $\bar{A}_a/\bar{A}_a^{min}$, and using the approximations (2.39) and (2.40) for $\bar{A}_a/\bar{A}_a^{min} \gg 1$, (3.17) yields

$$I_c = (8.53\text{kA})\bar{\kappa} = (8.53 \text{ kA})\frac{\kappa}{\ln(r_a/r_c)}$$

$$\approx \frac{8.53 \text{ kA}}{\ln(r_a/r_c)} \times \left(\frac{\bar{A}_a}{\bar{A}_a^{min}}\right)\gamma_a\beta_a \qquad (3.20)$$

$$I_e = I_a - I_c = I_c(\cosh(\chi_b) - 1) \approx I_c\chi_b^2/2$$

$$\approx I_c \times \left[\frac{1}{2}\left(\frac{\bar{V}_a}{\gamma_a\beta_a}\right)^2\left(\frac{1}{\bar{A}_a/\bar{A}_a^{min}}\right)^2\right]. \qquad (3.21)$$

Note that, once more, under this assumption of good magnetic insulation, $I_c \approx I_a \gg I_e$. We next assume that the MILO produces RF power from the potential energy drop experienced by the spoke electrons as they are transported across the AK gap from the top of the Brillouin hub, as in a magnetron. This maximum potential energy drop is clearly V_a, the AK gap voltage. We further assume that the maximum spoke current is the electron current I_e, carried in the Brillouin hub, as in a magnetron (realistically the spoke current is only a fraction of I_e; see Vaughan [35] for an estimate for conventional magnetrons). It follows that the maximum RF power that can be generated in a MILO is V_aI_e. The input power is V_aI_a. So,

the maximum efficiency in a MILO is I_e/I_a, which is typically at most a few percent, approximately given by the square bracket in (3.21). This square bracket shows very unfavorable efficiency scaling for a low-voltage ($\sim$50 kV) MILO [see also (2.38) and Fig. 7].

Below, we will give three examples of different types of MILOs, mentioned at the beginning of this section. In all examples, we set $\bar{A}_a/\bar{A}_a^{min} = 1.5$ for easy comparison. From (3.20), we note that the cathode current I_c depends only on $\ln(r_a/r_c)$, once V_a and $\bar{A}_a/\bar{A}_a^{min}$ are fixed.

1) High-Current MILO: In the literature, MILO experiments operated at high currents, typically on the order of 50 kA and beyond [3], [4], [20], [21], [25], [26], [28]. As an example, we take $V_a = 500$ kV and $\bar{A}_a/\bar{A}_a^{min} = 1.5$. We obtain $\kappa = 2.354$ and $\chi_b = 0.4451$ from Tables I and II. The normalized phase velocity for the synchronous operating mode is β_{ph}, where $\beta_{ph} = \beta_b = \tanh(\chi_b) = 0.4178$. If we further assume $r_a = 8.57$ cm, $r_c = 5.71$ cm, as in the brazed MILO [20], then (3.20) and (3.21) yield $I_c = 49.45$ kA, $I_a = 54.43$ kA, and $I_e = 4.98$ kA. In addition, the cathode magnetic field is $B_c = 1.732$ kG upon using (2.17) and (3.5). These numbers are in qualitative agreement with the experiments [20].

2) Moderate-Current MILO and MILO–Magnetron Hybrid: We now consider the feasibility of driving a "moderate-current" MILO using a MELBA-like accelerator, which operates at a current of order 10 kA [9]. We take $V_a = 300$ kV, and $\bar{A}_a/\bar{A}_a^{min} = 1.5$. We then obtain $\kappa = 1.746$ and $\chi_b = 0.3680$ from Tables I and II. The normalized phase velocity for the synchronous operating mode is β_{ph}, where $\beta_{ph} = \beta_b = \tanh(\chi_b) = 0.3522$. To reduce the cathode (and anode) current to the 10 kA range, we need to increase the aspect ratio, r_a/r_c, according to (3.20). So we take $r_c = 1$ cm, and $r_a = 6$ cm. This gives $I_c = 8.31$ kA, $I_a = 8.88$ kA (see Fig. 9), and $I_e = 0.57$ kA is the electron current carried in the Brillouin hub, whose hub radius is at $r_b = 1.459$ cm.

To see the effect of the aspect ratio on the cathode current, let us again set $V_a = 300$ kV, and $\bar{A}_a/\bar{A}_a^{min} = 1.5$, so that $\kappa = 1.746$ and $\chi_b = 0.3680$ is the same as before. So is $\beta_{ph} = \beta_b = \tanh(\chi_b) = 0.3522$. If we now take $r_c = 3$ cm and $r_a = 6$ cm then for a MILO that completely establishes its magnetic field through driven current, the cathode current required would be 21.48 kA according to (3.20), and the cathode magnetic field is $B_c = 1.432$ kG upon using (2.17) and (3.5). This cathode magnetic field then produces the desired degree of magnetic insulation, $\bar{A}_a/\bar{A}_a^{min} = 1.5$, that is, a total magnetic field roughly equal to 1.5 times the HC magnetic field. If the MELBA-like accelerator can only deliver 10 kA of axial current, to produce the same degree of magnetic insulation, an external magnetic field, B_z, will be required. This becomes a MILO–magnetron hybrid whose B_z is approximately given by

$$B_c^2 = \left(\frac{10 \text{ kA}}{21.48 \text{ kA}}\right)^2 B_c^2 + B_z^2 \qquad (3.22)$$

so that the azimuthal magnetic field due to 10-kA current, together with the externally imposed axial magnetic field B_z, would yield a total magnetic field equal to $B_c = 1.432$ kG

in magnitude. Equation (3.22) yields $B_z = 1.267$ kG. Such a high external magnetic field makes the MILO–magnetron hybrid example unattractive compared with simply increasing the aspect ratio, r_a/r_c [cf. (3.20)] to achieve the same degree of magnetic insulation at a given voltage V_a.

From Fig. 9, which assumes a high aspect ratio of $r_a/r_c = 6$, MELBA MILO operation is feasible at ~1.1 times the HC at ~10 kA currents without an axial magnetic field. MILO experiments were recently performed using MELBA with $V_a = 240$ kV, $I_a \cong 10$ kA, and $\bar{A}_a/\bar{A}_a^{\min} \cong 1.2$, guided by the design procedure given here [71], [72].

3) Low-Voltage MILO: Finally, let us examine the possibility of a MILO operating at a low voltage V_a. This is a rather tempting proposition because of the potential availability of an HPM device that operates without an external magnetic field and at a low voltage. Let us consider a low-voltage MILO with $V_a = 50$ kV, and once more, we assume $\bar{A}_a/\bar{A}_a^{\min} = 1.5$. We obtain $\kappa = 0.672$ and $\chi_b = 0.1654$ from Tables I and II. The normalized phase velocity for the synchronous operating mode is $\beta_{\rm ph}$, where $\beta_{\rm ph} = \beta_b = \tanh(\chi_b) = 0.1639$. If we take $r_c = 1$ cm, and $r_a = 2$ cm, then we obtain $I_c = 8.270$ kA, and $B_c = 1.654$ kG. These are all very reasonable for HPM sources. However, we also find that $I_a = 8.383$ kA, and $I_e = 0.113$ kA from (3.20) and (3.21). The very low electron current in the Brillouin hub, I_e, in comparison with the anode current, I_a, is due to the unfavorable scaling at low voltage, as indicated by the square bracket in (3.21). A low I_e necessarily implies a low spoke current, as spoke electrons are drawn from the Brillouin hub (if we assume the same spoke generation mechanism as in a magnetron). Thus, a MILO driven at a low voltage, though immensely attractive in practice, is unlikely to efficiently produce HPMs despite the availability of the low-impedance LTD. A higher cathode current would make the degree of insulation, $\bar{A}_a/\bar{A}_a^{\min}$, higher, the Brillouin hub height even smaller, further reducing I_e, as again implied by the scaling law (3.21). This predicted decrease in efficiency with decreasing applied voltage is supported by previous particle-in-cell simulations [22].

Since a low-voltage MILO is highly inefficient, we consider only $V_a > 200$ kV in Fig. 9, where we calculate the anode current I_a and the cathode current I_c in a cylindrical MILO at various degrees of magnetic insulation, $\bar{A}_a/\bar{A}_a^{\min}$, assuming an aspect ratio $r_a/r_c = 6$. The total electron current carried within the Brillouin hub is $I_e = I_a - I_c$, which can readily be obtained from Fig. 9.

IV. RADIALLY CONVERGING BRILLOUIN FLOW

The radially converging Brillouin flow in the LTD geometry is schematically shown in Fig. 1(c). This section gives the approximate Brillouin flow solution for this radial MITL, at each radius. The anode, located at $z = D$, is assumed to be held at a constant AK gap voltage, V_a, with respect to the cathode, which is located at $z = 0$ and is held at zero potential. The anode current, I_a, is assumed to be a constant (independent of r) and flows radially inward. Both V_a and I_a are treated as input parameters, independent of r. The assumption that the AK gap voltage does not vary strongly with radius is valid as

long as the load impedance is large and/or the current pulse is not rapidly rising or falling, meaning that the radially dependent inductive voltage $V_L(r) = L(r)dI_a/dt$ is relatively small compared to the resistive or space–charge-limited voltage drop across the load. The Brillouin electron flow, whose hub height at $r = R$ is denoted as z_b for Fig. 1(c), flows radially inward, carrying a total electron current of magnitude I_e that flows radially outward. The current on the cathode, I_c, also flows radially outward. The magnetic field is in the θ-direction. For a radially converging anode current, the magnetic field is a function of radius r, so is the Brillouin hub height, the Brillouin flow profile, and the total electron current, I_e. The cathode current I_c is also a function of radius r, but their sum, $I_e + I_c = I_a$, is the pre-assigned constant. We shall seek to determine the Brillouin flow profile as a function r, at some typical radius $r = R$, with $R \gg D$. This assumption allows us to use the Cartesian, planar Brillouin flow that was studied in great detail in Section II, as a local approximation to the radial Brillouin flow. This local approximation is expected to be the lowest order approximation in an asymptotic analysis using R/D as an expansion parameter, $R/D \gg 1$.

For $R \gg D$, the cylindrical geometry in the directions (r, θ, z) in Fig. 1(c) may be approximated by the local Cartesian geometry in Fig. 1(a), respectively, in the directions (y, z, x). The height, W, in the Cartesian geometry [in the z-direction in Fig. 1(a)] then becomes

$$W = 2\pi R \quad (4.1)$$

so that the surface current density (in A/m) at the anode and at the cathode is, respectively,

$$K_a = I_a/(2\pi R) = H_a = B_a/\mu_0 \quad (4.2)$$
$$K_c = I_c/(2\pi R) = H_c = B_c/\mu_0 \quad (4.3)$$

which clearly show that the magnetic field is a function of R. In (4.2) and (4.3), H and B are to be evaluated at the anode and at the cathode, at the radius $r = R$. As in Sections II and III, we will use the normalized gap voltage $\bar{V}_a$ and the local normalized vector potential (or flux function) $\bar{A}_a$ to determine the Brillouin flow properties. The radius R, for that local normalized vector potential $\bar{A}_a$, will then be determined for the pre-assigned value of I_a.

For the normalized gap voltage $\bar{V}_a$, we define γ_a and β_a by (2.27) and the minimum magnetic flux $\bar{A}_a^{\min} = \gamma_a \beta_a$ for magnetic insulation [cf. (2.28)]. Now choose a value of $\bar{A}_a$ which satisfies

$$\bar{A}_a > \bar{A}_a^{\min} = \gamma_a \beta_a. \quad (4.4)$$

We shall determine below, (4.7), the value of radius R that corresponds to this assigned value of $\bar{A}_a$.

With $\bar{V}_a$ and a value of $\bar{A}_a$ given in (4.4), we compute χ_b from (2.26), κ by (2.29), both having been given in Figs. 3 and 4, and tabulated in Tables I and II. The normalized hub height is $\bar{z}_b = \chi_b/\kappa$ by (2.30), the normalized Brillouin flow speed at the top of the hub is $\beta_b = \tanh(\chi_b)$ according to (2.12), and the normalized magnetic field at the anode and cathode become, by (2.17),

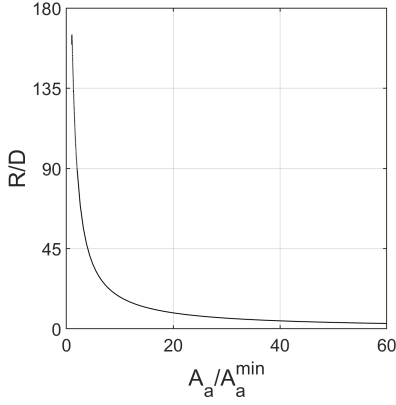$$\bar{H}_a = \bar{B}_a = \bar{K}_a = \kappa \cosh(\chi_b) \quad (4.5)$$

Fig. 10. Relation between R/D and the degree of magnetic insulation, for $R/D > 3$, in a radial MITL [Fig. 1(c)] with $V_a = 100$ kV, $D = 1$ cm, $I_a = 1$ MA. At each value of R/D, the value of $\bar{A}_a/\bar{A}_a^{\min}$ given here will be used to construct Figs. 11–16. Note that over much of the region shown, $\bar{A}_a/\bar{A}_a^{\min} > 2$, and that the MITL is very deeply insulated magnetically for smaller values of R.

$$\bar{H}_c = \bar{B}_c = \bar{K}_c = \kappa. \qquad (4.6)$$

Equation (4.2) then gives

$$R = \frac{I_a}{2\pi H_a} = \frac{D}{2\pi}\left(\frac{I_a}{I_s}\right)\frac{1}{\kappa \cosh(\chi_b)} \qquad (4.7)$$

where we have used (4.5) and $I_s = 1.358$ kA by (1.4). The relation between the radius R and $\bar{A}_a/\bar{A}_a^{\min}$ as given by (4.7) is plotted in Fig. 10 for an LTD example (similar to one at the University of Michigan [37]), with $V_a = 100$ kV, $D = 1$ cm, $I_a = 1$ MA. In other words, given these three quantities, (V_a, D, I_a), the radius R that would give a certain degree of magnetic insulation as measured by $\bar{A}_a/\bar{A}_a^{\min}$, is explicitly given by (4.7). At that radius, the ratio between the anode current (I_a), the cathode current (I_c), and the electron current carried by the Brillouin hub (I_e), all defined positive by convention, is given by (2.38).

We next determine the radius, $R = R_m$, at which $\bar{A}_a/\bar{A}_a^{\min} = 1$, that is, the top of the Brillouin hub barely touches the anode at $R = R_m$. This corresponds to $\bar{x}_b = 1$ in the Cartesian approximation, and (2.19) gives $\kappa = \chi_b$, whereas (2.13) implies $\cosh(\chi_b) = \gamma_b = \gamma_a$. Equation (4.7) then gives

$$R_m = \frac{D}{2\pi}\left(\frac{I_a}{I_s}\right)\frac{1}{\gamma_a \cosh^{-1}\gamma_a}. \qquad (4.8)$$

We note here that, as the (constant) anode current flows radially inward passing through this radius, $R = R_m$, the MITL transitions from nonmagnetic insulation to magnetic insulation, which will be discussed further below. A similar transition might also have occurred spatially in a MILO experiment, but this was not included in the analytical model in Section III.

Using the LTD parameters quoted above, $V_a = 100$ kV, $D = 1$ cm, $I_a = 1$ MA, we obtain $R_m = 1.595$ m from (4.8). Since $R_m \gg D$, we are fully justified to approximate the radial MITL geometry as Cartesian, locally, as we have done here. We plot in Figs. 11–16 the values of χ_b, κ, $\bar{z}_b$, β_b, ϕ_b, and I_e/I_a, as a function of R for $R > 3D$. In Figs. 11–16, we set $V_a = 100$ kV, $D = 1$ cm, $I_a = 1$ MA,
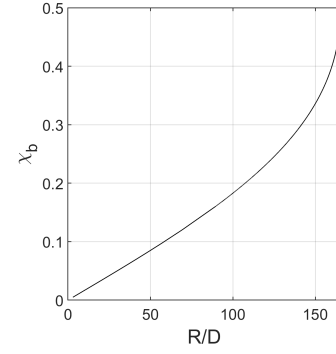

Fig. 11. Parameter χ_b as a function of R/D for $R/D > 3$, in a radial MITL [Fig. 1(c)] with $V_a = 100$ kV, $D = 1$ cm, $I_a = 1$ MA.
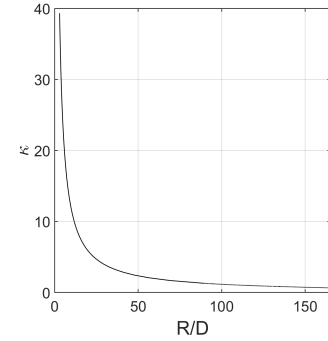

Fig. 12. Parameter κ as a function of R/D for $R/D > 3$, in a radial MITL [Fig. 1(c)] with $V_a = 100$ kV, $D = 1$ cm, $I_a = 1$ MA.
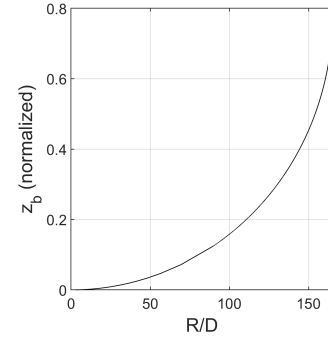

Fig. 13. Normalized Brillouin hub height $\bar{z}_b$ as a function of R/D for $R/D > 3$, in a radial MITL [Fig. 1(c)] with $V_a = 100$ kV, $D = 1$ cm, $I_a = 1$ MA. Note the very thin Brillouin hub height for $R/D < 75$.

and for each R, we use the value of $\bar{A}_a/\bar{A}_a^{\min}$ given in Fig. 10. All parameters in Figs. 11–16 are then determined assuming a local Cartesian Brillouin flow [Fig. 1(a)] and explicitly computed in detail in Section II. We anticipate that these Cartesian solutions are excellent approximations for the radial MITL for $R/D > 3$, as "3" is, in practice, a sufficiently large parameter in an asymptotic analysis.

Finally, we remark that, in the immediate vicinity of marginal magnetic insulation ($\bar{A}_a/\bar{A}_a^{\min} = 1$), one value of K_a may correspond to two values of $\bar{A}_a/\bar{A}_a^{\min}$, as shown by the V-shaped curves in Fig. 8(a) and proved in Appendix A, where we also discuss some subtlety of this double-valuedness. For this reason, we use only the right branch of the
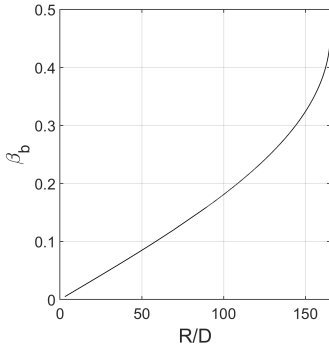
Fig. 14. Normalized electron velocity at the top of the Brillouin hub, β_b, as a function of R/D for $R/D > 3$, in a radial MITL [Fig. 1(c)] with $V_a = 100$ kV, $D = 1$ cm, $I_a = 1$ MA.
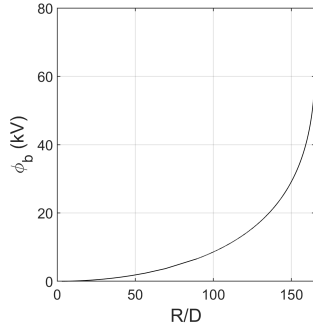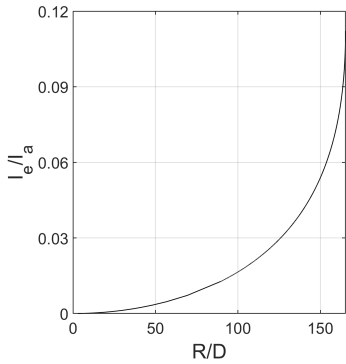

Fig. 15. Electron kinetic energy, which equals to its potential energy in magnitude, ϕ_b, at the top of the Brillouin hub, as a function of R/D for $R/D > 3$, in a radial MITL [Fig. 1(c)] with $V_a = 100$ kV, $D = 1$ cm, $I_a = 1$ MA. Note the very low kinetic energy for $R/D < 75$.

Fig. 16. Ratio of the electron current within the Brillouin hub to the anode current, as a function of R/D for $R/D > 3$, in a radial MITL [Fig. 1(c)] with $V_a = 100$ kV, $D = 1$ cm, $I_a = 1$ MA. Note that this ratio is very small for all R, meaning that the electrons within the Brillouin hub contribute only a very small self-magnetic field toward magnetic insulation.

above-mentioned V-shaped curve [Fig. 8(a)], down to the minimum of this V-shaped curve, when we construct Figs. 11–16, as R/D increases from 3. The nature of this V-shaped curve deserves further attention. This is especially true when the MILO operates close to HC [71], [72].

V. Cylindrical Brillouin Flow in Azimuthal Direction

The Brillouin flow is in the azimuthal direction for a cylindrical magnetron [Fig. 1(d)]. In the relativistic regime, this problem was studied in [46] and [69]. For completeness,

we include it here using our formulation and notation, in terms of $\bar{V}_a$ and $\bar{A}_a$. The magnetic field is in the axial direction, and the electric field is in the radial direction [Fig. 1(d)]. The anode radius is r_a, which will be used as the distance scale [cf. (1.11)], and the cathode radius is r_c, with the aspect ratio $\bar{r}_c = r_c/r_a < 1$. For the relativistic azimuthal Brillouin flow, there is no analytic, closed-form solution for the flow profile. The flow profile must be obtained numerically, as detailed in [69], where it is shown that the BH condition according to the Brillouin flow model is markedly different from the single-particle orbit model (3.19), [69], [70] that was commonly used in the literature, for both conventional and relativistic *cylindrical* magnetrons. To facilitate comparison with other Brillouin flow solutions shown in Fig. 1(a)–(c), we outline below the Brillouin flow solution and the BH condition for a cylindrical magnetron [Fig. 1(d)], using this article's notation.

Given the normalized gap voltage $\bar{V}_a$, the normalized total axial magnetic flux in the AK gap, $\bar{A}_a$ (or equivalently the degree of magnetic insulation $\bar{A}_a/\bar{A}_a^{\min}$ where $\bar{A}_a^{\min}$ is given by (2.28) as in Sections II–IV), and the aspect ratio $\bar{r}_c$, we need to numerically solve for the three parameters, $(\bar{r}_b, \bar{\kappa}, \chi_b)$, from the following three equations:

$$\bar{V}_a = \cosh(\chi_b) - 1 + \sinh(\chi_b)\sqrt{\bar{\kappa}^2 + \sinh^2(\chi_b)} \times \ln(1/\bar{r}_b) \tag{5.1}$$

$$\bar{A}_a = \frac{1}{2\bar{r}_b}\left[\left(1 + \bar{r}_b^2\right)\sinh(\chi_b) \right.$$
$$\left. + \left(1 - \bar{r}_b^2\right)\cosh(\chi_b)\sqrt{\bar{\kappa}^2 + \sinh^2(\chi_b)}\right] \tag{5.2}$$

$$\ln\left(\frac{\bar{r}_b}{\bar{r}_c}\right) = \int_0^{\chi_b} d\chi/\sqrt{\bar{\kappa}^2 + \sinh^2(\chi)}. \tag{5.3}$$

Equations (5.1)–(5.3) are the same as (7)–(9) of [69], whose Appendix B presented an algorithm to solve for $(\bar{r}_b, \bar{\kappa}, \chi_b)$. From these values, we next obtain the relation between χ and $\bar{r}$, that is, $\chi = \chi(\bar{r})$, through the relation

$$\ln\left(\frac{\bar{r}}{\bar{r}_c}\right) = \int_0^{\chi} d\chi/\sqrt{\bar{\kappa}^2 + \sinh^2(\chi)}, \quad \bar{r}_c < \bar{r} < \bar{r}_b. \tag{5.4}$$

The Brillouin flow fields, for $\bar{r}_c < \bar{r} < \bar{r}_b$, are then given by (2.12)–(2.15), copied here for emphasis of their generality

$$\beta = \tanh(\chi) \tag{5.5}$$
$$\gamma = \cosh(\chi) \tag{5.6}$$
$$\bar{\phi} = \cosh(\chi) - 1 \tag{5.7}$$
$$\bar{A} = \sinh(\chi). \tag{5.8}$$

Equations (5.4) and (5.5) are the same as (10) and (11) of [69], respectively.

The HC condition, according to the Brillouin flow model, is obtained by setting $\bar{r}_b = 1$ in (5.1) and (5.2), which yields (2.31).

For the BH condition, we consider an operating mode whose phase velocity *at the anode* is $v_{\mathrm{ph}} = c\beta_{\mathrm{ph}}$ in the azimuthal direction. This azimuthal phase velocity, at the top of the Brillouin hub, becomes $(r_b/r_a)v_{\mathrm{ph}} = \bar{r}_b c\beta_{\mathrm{ph}}$, which is to be

equated with the Brillouin flow velocity at $r = r_b$ to obtain BH. The BH according to the Brillouin flow model then reads

$$\beta_{\text{ph}} \bar{r}_b = \tanh(\chi_b) \qquad (5.9)$$

upon using (5.5) evaluated at $\bar{r}_b$. Equation (5.9) is the same as (13) of [69] whose Appendix B also provides the algorithm to solve (5.9). We should stress that β_{ph} in (5.9) is the normalized phase velocity of the operating mode evaluated at the anode.

For the aspect ratio $\bar{r}_c = r_c/r_a < 1/2$, (5.9) shows significant deviation from the BH condition shown in Fig. 2, which is also the BH for the cylindrical magnetron according to the single-particle orbit model [70], [11], [69]. Fig. 8 of [69] shows that the experimental data from the University of Michigan relativistic magnetron could not be interpreted in terms of the BH condition according to the single-particle orbit model, but are consistent with the BH according to the Brillouin flow model. Simon [73] also found that the simulation data of an inverted relativistic magnetron [74] could not be explained in terms of the BH condition according to the single-particle orbit model, but are consistent with the BH condition according to the Brillouin flow model.

VI. CONCLUDING REMARKS

In this article, we derive the Brillouin flow solutions for the four geometries described in Fig. 1. The AK gap voltage, the degree of magnetic insulation, and the geometrical aspect ratio in the case of cylindrical geometry completely characterize the Brillouin flow solutions, whether the magnetic field is provided by an external magnet, by the wall currents, or by a mixture of the two, as in a magnetron–MILO hybrid. The Brillouin flow profiles are explicitly calculated. The BH condition and the HC condition are derived from this Brillouin flow model. Various scaling laws are derived, from which new insights are offered.

In a magnetron, it is commonly accepted that the electron spokes are generated from the Brillouin flow, and the spoke current is only a fraction of the electron current carried within the Brillouin electron hub. In this article, we assume the same scenario for the MILO in an analytical theory, which is a natural starting point to develop a MILO theory that can be more readily compared with the magnetron theory. From this assumption, we deduce that the MILO efficiency cannot be much beyond 5 percent and is even less for a low-voltage MILO. We are aware that in MILO experiments, the spoke current may exceed the Brillouin flow current by a large amount, implying the electron spokes in a MILO might not have originated from the Brillouin flow and therefore might achieve much higher power and efficiency experimentally than those predicted based on the Brillouin flow picture that is given in this article. If the MILO does generate spoke current much higher than the electron current within the Brillouin flow (by some unspecified mechanism), the hope remains for a low-voltage MILO to be built, possibly with an operating voltage as low as 50 kV.

Since magnetic insulation is quickly lost once $\bar{A}_a/\bar{A}_a^{\text{min}} \rightarrow 1$, the region of $\bar{A}_a/\bar{A}_a^{\text{min}} \cong 1$ deserves close attention. The V-shape shown in the anode current versus

$\bar{A}_a/\bar{A}_a^{\text{min}}$ curves, for MILO or MITL as shown in Fig. 8(a), occurs around $\bar{A}_a/\bar{A}_a^{\text{min}} \cong 1$, and this V-shape nature has affected our construction of the Brillouin flow solutions in the radial MITL. It is of interest to ponder if this V-shape is somehow related to the unexpectedly large spoke currents observed in MILO experiments and simulations. Indeed, MILO might operate at a rather low value of $\bar{A}_a/\bar{A}_a^{\text{min}}$, such as 1.1, which is very different from the operation of a magnetron or a relativistic magnetron [71], [72].

Finally, when the MITL is magnetically well insulated, $\bar{A}_a/\bar{A}_a^{\text{min}}$ is large, the Brillouin hub height is very small, and the Brillouin flow is non-relativistic, regardless of the voltage and geometry. Under such a condition, we may consider the Brillouin flow to be planar and non-relativistic, in which case the diocotron instability is well studied. (The diocotron instability has also been known as the slipping-stream instability or Kelvin–Helmholtz instability. See Table I of Buneman *et al.* [61].) We may then reassess the leakage current on a MITL, caused by cathode surface roughness, for instance, which could seed the diocotron instability. Note that the diocotron instability has long been suspected to be a candidate to initiate startup of the magnetron oscillation, or as a source of excessive noise in crossed-field devices [9], [34], [43], [44], [61].

APPENDIX A
ASYMPTOTIC BEHAVIOR OF PLANAR BRILLOUIN FLOW

In this appendix, we derive the asymptotic formulas, (2.39)–(2.46), under the assumption $\bar{A}_a/\bar{A}_a^{\text{min}} \gg 1$. We shall also give the behaviors of these quantities as $\bar{A}_a/\bar{A}_a^{\text{min}} \rightarrow 1$. Toward the end of this appendix, we further discuss several important properties from these scaling laws to support the claims in the main text.

At a fixed value of $\bar{V}_a$, for $\bar{A}_a/\bar{A}_a^{\text{min}} \gg 1$, the Brillouin hub height is very small because the crossed-field diode is deeply magnetically insulated. The normalized Brillouin flow velocity β_b at the top of the Brillouin hub is expected to be a small number, that is, this velocity is deeply non-relativistic because the flow velocity is constrained to be zero on the cathode surface. If $\beta_b = \tanh(\chi_b) \ll 1$, this implies that, for $\bar{A}_a/\bar{A}_a^{\text{min}} \gg 1$

$$\chi_b \ll 1. \qquad (A.1)$$

Using (A.1) in the hyperbolic functions in (2.25) [or, equivalently, (C.1) of Appendix C], we obtain, to the lowest order

$$\chi_b \approx \bar{V}_a/\bar{A}_a \qquad (A.2)$$

which is (2.39). Likewise, using (A.1) in (2.29), we obtain, to the lowest order

$$\kappa \approx \bar{A}_a \qquad (A.3)$$

which is (2.40). These approximate formulas for χ_b and κ are plotted in Figs. 3 and 4, with their comparison with the exact values given in Tables I and II. Note that these two parameters are independent of geometries and therefore they are applicable to all geometries in Fig. 1(a)–(c).

Using (A.1)–(A.3) in (2.30), (2.34), (2.14), and (2.35), we obtain, respectively, (2.41), (2.42), (2.43), and (2.44). Equations (2.45) and (2.46) then follow from (2.44) and (2.38).

While the approximate formulas, (2.39)–(2.46), are derived asymptotically assuming $\bar{A}_a \to \infty$, Figs. (3)–(8) show that all of these asymptotic formulas are very accurate as long as $\bar{A}_a/\bar{A}_a^{\min} > 3$. This observation encouraged us to approximate the radial Brillouin flow profile in the MITL [Fig. 1(c)] as locally a Cartesian Brillouin flow over the vast region $R/D > 3$, where R is the radius from the center line and D is the AK gap spacing, as in Section IV. Both $\bar{A}_a/\bar{A}_a^{\min}$ and R/D are treated as dimensionless expansion parameters.

As $\bar{A}_a/\bar{A}_a^{\min} \to 1$, the Brillouin hub is about to touch the anode. All quantities plotted in Figs. 3–8 have a finite limit at $\bar{A}_a/\bar{A}_a^{\min} = 1$, their values are given in (A.4)–(A.10). Also given in (A.4)–(A.10) are the slopes of these curves as $\bar{A}_a/\bar{A}_a^{\min} \to 1$

$$\chi_b = \cosh^{-1}(\gamma_a), \quad \partial\chi_b/\partial\bar{A}_a \to -\infty \tag{A.4}$$

$$\kappa = \cosh^{-1}(\gamma_a), \quad \partial\kappa/\partial\bar{A}_a \to \gamma_a^3/2 \tag{A.5}$$

$$\bar{x}_b = 1, \quad \partial\bar{x}_b/\partial\bar{A}_a \to -\infty \tag{A.6}$$

$$\beta_b = \beta_a, \quad \partial\beta_b/\partial\bar{A}_a \to -\infty \tag{A.7}$$

$$\bar{\phi}_b = \bar{V}_a, \quad \partial\bar{\phi}_b/\partial\bar{A}_a \to -\infty \tag{A.8}$$

$$\bar{K}_a = \bar{B}_a = \bar{B}_b = \gamma_a\cosh^{-1}(\gamma_a),$$
$$\partial\bar{K}_a/\partial\bar{A}_a \to -\infty \tag{A.9}$$

$$\bar{K}_e = \bar{V}_a\cosh^{-1}(\gamma_a), \quad \partial\bar{K}_e/\partial\bar{A}_a \to -\infty \tag{A.10}$$

$$I_a : I_c : I_e = (1 + \bar{V}_a) : 1 : \bar{V}_a. \tag{A.11}$$

To derive (A.4), we note that as the top of Brillouin hub is about to touch the anode, (2.13) gives $\cosh(\chi_b) = \gamma_a$ which is the first part of (A.4). To derive the second part of (A.4), we differentiate (2.34) with respect to $\bar{A}_a$, holding $\bar{V}_a$ (and therefore $\bar{A}_a^{\min}$) fixed. The last term gives $(\partial\chi_b/\partial\bar{A}_a)/\cosh^2(\chi_b)$. The middle term gives, in the limit $\bar{A}_a/\bar{A}_a^{\min} \to 1$, $-[\bar{A}_a/(\bar{A}_a^2 + 1)]/(\bar{A}_a^2 - (\bar{A}_a^{\min})^2)^{1/2}$. Equating these two terms, we obtain the slope of χ_b as $\bar{A}_a/\bar{A}_a^{\min} \to 1$ in Fig. 3:

$$\frac{\partial\chi_b}{\partial\bar{A}_a} \cong -\left[\frac{\gamma_a^2\bar{A}_a}{\bar{A}_a^2 + 1}\right]\frac{1}{\sqrt{\bar{A}_a^2 - (\bar{A}_a^{\min})^2}} \to -\infty, \tag{A.12}$$
$$\bar{A}_a/\bar{A}_a^{\min} \to 1.$$

Equation (A.4), in particular, the negative infinite slope of χ_b at $\bar{A}_a/\bar{A}_a^{\min} = 1$, are present in all solid curves in Fig. 3. The remaining equations, (A.5)–(A.10), may be similarly proved upon using, respectively, (2.29), (2.24), (2.12), (2.14), (2.35), and (2.38). Note that (A11) follows from (2.38); it is valid *only* when $\bar{A}_a/\bar{A}_a^{\min} = 1$.

We next make a few remarks on the negative infinite slopes, and the values of several quantities, at $\bar{A}_a/\bar{A}_a^{\min} = 1$.

1) From (A.6), and Fig. 5, we see that the top of the Brillouin hub rapidly approaches the anode as $\bar{A}_a/\bar{A}_a^{\min} \to 1$. This corresponds to the well-known fact that magnetic insulation in a crossed-field gap is quickly lost as the magnetic field approaches the HC value [8].

2) Equation (2.44) shows that the anode current $\bar{K}_a$ increases with $\bar{A}_a$ at large values, whereas (A.9) shows

that $\bar{K}_a$ decreases rapidly as $\bar{A}_a$ slightly exceeds $\bar{A}_a^{\min}$. The underlying reason is that, as magnetic insulation is lost, $\bar{K}_e$ rapidly increases (Fig. 8(b)), $\bar{K}_c$ remains a constant, (see (4.6) and Fig. 4), and $\bar{K}_a = \bar{K}_e + \bar{K}_c$. Thus, the curve of $\bar{K}_a$ as a function of $\bar{A}_a$ must have a V-shape near the HC, as shown in Fig. 8(a), regardless of the value of $\bar{V}_a$. This means that, in a MILO or MITL, magnetic insulation ($\bar{A}_a/\bar{A}_a^{\min} > 1$) may be achieved at a value of anode current less than the value corresponding to HC ($\bar{A}_a/\bar{A}_a^{\min} = 1$). This unexpected result is evident in the top curve (in green) in Fig. 8(a). It was also noted in Packard's recent MILO experiments [71], [72]. We again encountered this double-valued problem when we treated the radial MITL [Fig. 1(c)] in Sect IV. In the radial MITL, if we fix the total anode current (and the AK gap voltage), we will follow only the right half branch of the V-shape curve in Fig. 8(a) as the radius R increases, that is, as $\bar{A}_a/\bar{A}_a^{\min}$ decreases (see Fig. 10). This issue is addressed in Section IV.

3) In a MILO or MITL operating with a gap voltage on the order of hundreds of kV, which is within the common range of the operating voltages, (A.11) shows that the cathode current (I_c) and the total electron current carried within the Brillouin hub (I_e) are of the same order of magnitude. This might have led to the misconception that the electron current contributes significantly to magnetic insulation in a MILO and MITL. These two currents are of the same order of magnitude *only when* the diode is marginally magnetically insulated, that is, only when $\bar{A}_a/\bar{A}_a^{\min} \cong 1$. For a deeply (and even not so deeply) magnetically insulated diode, I_e is much less than I_c, as shown in the scaling law (2.46) [see also the exact expression (2.38) and Figs. 7 and 16]. Thus, the electron current within the Brillouin hub contributes little toward magnetic insulation in a MITL or MILO.

APPENDIX B
HC AND BH CONDITION IN A CYLINDRICAL MILO FROM THE SINGLE-PARTICLE ORBIT MODEL

In this Appendix, we derive the HC condition and the BH condition for the cylindrical MILO, according to the cycloidal orbit, single-particle model. We show that they are the same as the Brillouin flow model, given by (3.18) and (3.19), respectively, and plotted in Fig. 2.

In the single-particle orbit model for the cylindrical MILO [Fig. 1(b)], an electron released from the cathode surface at $r = r_c$ with zero initial kinetic and potential energy will move radially outward, execute a cycloidal motion by acquiring a z-component velocity before it returns to the cathode. The three components of the electron velocity are $(v_r, v_\theta, v_z) = c(\beta_r, 0, \beta_z)$. Including the space charge effect and space current effect, $\bar{\phi}$ is governed by Poisson's equation (3.2), and $\bar{A}$ is governed by Ampere's law (3.3) in which β is replaced by β_z.

To derive the HC condition, energy conservation for the emitted electron gives

$$\bar{\phi} = \gamma - 1, \gamma = 1/\sqrt{1 - \beta_r^2 - \beta_z^2}. \tag{B.1}$$

Conservation of the z-component of the canonical momentum for that electron gives

$$\bar{A} = \gamma \beta_z \qquad (\text{B.2})$$

where we have again used the convention that all quantities, $(\bar{\phi}, \bar{A}, \beta_r, \beta_z)$, are positive. Note that (B.1) and (B.2) satisfy the initial condition for this electron, $\bar{\phi} = \bar{A} = \beta_r = \beta_z = 0$, on the cathode. The HC condition is reached when this electron barely touches the anode, at which $\beta_r = 0$, $\beta_z = (1 - 1/\gamma^2)^{1/2}$, and (B.1) and (B.2) become

$$\bar{V}_a = \gamma_a - 1 \qquad (\text{B.3})$$

$$\bar{A}_a = \gamma_a \beta_z = (\gamma_a^2 - 1)^{1/2} = \sqrt{\bar{V}_a^2 + 2\bar{V}_a} \qquad (\text{B.4})$$

where we have used the boundary conditions (2.8) and (2.9). Equation (B.4) is the same as the HC condition (3.18) which was derived from the Brillouin flow model. Note that (B1)–(B4) remain valid even if there is an arbitrary charge distribution in the AK gap that depends only on r [32], [69], [70].

To derive the BH condition, we follow [69] and [70] and assume that there is a small amplitude wave propagating in the z-direction with phase velocity v_{ph}. This wave provides a torque to bring the emitted electron from the cathode to the anode (despite magnetic insulation), but without changing its energy. The BH condition states that when this electron reaches the anode, it is trapped by this wave, that is, it co-moves with the wave. Thus, in the frame co-moving with the wave in the z-direction, at the constant velocity

$$\vec{v} = \hat{z} v_{\text{ph}} \qquad (\text{B.5})$$

this electron is at rest when it reaches the anode. Hereafter, we consider the electron dynamics in this moving frame. In this moving frame, the initial energy of the electron is

$$W_i = \gamma_{\text{ph}} mc^2 \qquad (\text{B.6})$$

$$\gamma_{\text{ph}} = 1/\sqrt{1 - \beta_{\text{ph}}^2}, \quad \beta_{\text{ph}} = v_{\text{ph}}/c. \qquad (\text{B.7})$$

This initial energy, W_i, includes the electron's rest energy mc^2.

The electric field and the transverse coordinates in the moving frame (primed quantities) are related to those in the lab frame (unprimed quantities) by the Lorentz transformation [80]

$$\vec{E}'_\perp = \gamma_{\text{ph}} \left(\vec{E}_\perp + \vec{v} \times \vec{B} \right) \qquad (\text{B.8})$$

$$\vec{x}'_\perp = \vec{x}_\perp, \quad r' = r \qquad (\text{B.9})$$

where the "$\perp$" sign refers to the direction perpendicular to z, which is mainly the radial direction for the present problem [Fig. 1(b)]. Thus, the radial component of (B.8) reads

$$E'_r = \gamma_{\text{ph}} (E_r - v_z B_\theta) = \gamma_{\text{ph}} \left(\frac{d\phi}{dr} - v_{\text{ph}} \frac{dA}{dr} \right) \qquad (\text{B.10})$$

where we have represented the electric (magnetic) field in terms of the scalar (vector) potential $\phi(A)$. At the anode, the kinetic energy the electron is zero in the moving frame, because the electron co-moves with the wave. The total energy of this electron at the anode, W_f, then consists of its rest energy, and the work done by E'_r on the electron as the electron moves radially from the cathode to the anode

$$W_f = mc^2 - e \int_{r_c}^{r_a} dr\, E'_r = mc^2 - e\gamma_{\text{ph}} (V_a - v_{\text{ph}} A_a). \qquad (\text{B.11})$$

In writing the last equality, we have used (B.10) and the boundary conditions (2.8) and (2.9) for ϕ and A. Equating (B.6) with (B.11), we obtain

$$\gamma_{\text{ph}} = 1 - \gamma_{\text{ph}} (\bar{V}_a - \beta_{\text{ph}} \bar{A}_a). \qquad (\text{B.12})$$

This equation may be written as, using (B.7),

$$\bar{V}_a = \bar{A}_a \beta_{\text{ph}} + \left[\sqrt{1 - \beta_{\text{ph}}^2} - 1 \right] \qquad (\text{B.13})$$

which is the same as the BH condition, (3.19), derived from the Brillouin flow model.

APPENDIX C
CLOSED-FORM SOLUTION TO (2.25)

To prove that (2.26) is the solution to (2.25), we first simplify (2.25) to read

$$\bar{A}_a - \frac{\gamma_a}{\tanh(\chi_b)} = -\frac{1}{\sinh(\chi_b)}. \qquad (\text{C.1})$$

Take the square of (C.1). This becomes a second-degree polynomial in $\tanh(\chi_b)$, easily solved to yield

$$\chi_b = \tanh^{-1} \left[\frac{\gamma_a \bar{A}_a \pm \sqrt{\bar{A}_a^2 + 1 - \bar{\gamma}_a^2}}{\bar{A}_a^2 + 1} \right] \qquad (\text{C.2})$$

which is (2.26) upon choosing the negative sign in front of the square root to ensure that $\beta_b = \tanh(\chi_b) < \beta_a$.

REFERENCES

[1] M. C. Clark, B. M. Marder, and L. D. Bacon, "Magnetically insulated transmission line oscillator," *Appl. Phys. Lett.*, vol. 52, no. 1, pp. 78–80, Jan. 1988, doi: 10.1063/1.99330.

[2] G. Bekefi and T. J. Orzechowski, "Giant microwave bursts emitted from a field-emission, relativistic-electron-beam magnetron," *Phys. Rev. Lett.*, vol. 37, no. 6, pp. 379–382, Aug. 1976, doi: 10.1103/PhysRevLett.37.379.

[3] J. Benford, J. A. Swegle, and E. Schamiloglu, *High Power Microwaves*. Boca Raton, FL, USA: CRC Press, 2015.

[4] R. J. Barker, N. C. Luhmann, J. H. Booske, and G. S. Nusinovich, *Modern Microwave and Millimeter Wave Power Electronics*. Piscataway, NJ, USA: IEEE, 2004.

[5] V. L. Granatstein and I. Alexeff, *High-Power Microwave Sources*. Norwood, MA, USA: Artech House, 1987.

[6] S. E. Tsimring, *Electron Beams and Microwave Vacuum Electronics*. Hoboken, NJ, USA: Wiley, 2006.

[7] J. Benford, "History and future of the relativistic magnetron," in *Proc. Int. Conf. Origins Evol. Cavity Magnetron*, Apr. 2010, pp. 40–45, doi: 10.1109/CAVMAG.2010.5565566.

[8] Y. Y. Lau, "Theory of crossed-field devices and a comparative study of other radiation sources," in *High-Power Microwave Sources*, V. L. Granatstein and I. Alexeff, Eds. Norwood, MA, USA: Artech House, 1987, ch. 9, pp. 309–351.

[9] R. M. Gilgenbach, Y. Y. Lau, H. McDowell, K. L. Cartwright, and T. A. Spencer, "Crossed field devices," in *Modern Microwave and Millimeter-Wave Power Electronics*. Hoboken, NJ, USA: Wiley, 2005. Accessed: Dec. 14, 2020. [Online]. Available: https://ieeexplore.ieee.org/book/5769526

[10] D. Andreev, A. Kuskov, and E. Schamiloglu, "Review of the relativistic magnetron," *Matter Radiat. Extremes*, vol. 4, no. 6, Nov. 2019, Art. no. 067201, doi: 10.1063/1.5100028.

[11] A. Palevsky and G. Bekefi, "Microwave emission from pulsed, relativistic e-beam diodes. II. The multiresonator magnetron," *Phys. Fluids*, vol. 22, no. 5, pp. 986–996, May 1979, doi: 10.1063/1.862663.

[12] T. Treado, "Generation and diagnosis of long- and short-pulse, high-power microwave radiation from relativistic rising-sun and A6 magnetrons," Ph.D. dissertation, North Carolina State Univ., Raleigh, NC, USA, 1989.

[13] J. W. Eastwood, K. C. Hawkins, and M. P. Hook, "The tapered MILO," *IEEE Trans. Plasma Sci.*, vol. 26, no. 3, pp. 698–713, Jun. 1998, doi: 10.1109/27.700810.

[14] D. E. T. F. Ashby, J. W. Eastwood, J. Allen, K. C. Hawkins, and L. M. Lea, "Comparison between experiment and computer modeling for simple MILO configurations," *IEEE Trans. Plasma Sci.*, vol. 23, no. 6, pp. 959–969, Dec. 1995, doi: 10.1109/27.476484.

[15] M. D. Haworth et al., "Significant pulse-lengthening in a multigigawatt magnetically insulated transmission line oscillator," *IEEE Trans. Plasma Sci.*, vol. 26, no. 3, pp. 312–319, Jun. 1998, doi: 10.1109/27.700759.

[16] M. D. Haworth, J. W. Luginsland, and R. W. Lemke, "Evidence of a new pulse-shortening mechanism in a load-limited MILO," *IEEE Trans. Plasma Sci.*, vol. 28, no. 3, pp. 511–516, Jun. 2000, doi: 10.1109/27.887660.

[17] M. D. Haworth, J. W. Luginsland, and R. W. Lemke, "Improved cathode design for long-pulse MILO operation," *IEEE Trans. Plasma Sci.*, vol. 29, no. 2, pp. 388–392, Apr. 2001, doi: 10.1109/27.922751.

[18] M. D. Haworth, K. L. Cartwright, J. W. Luginsland, D. A. Shiffler, and R. J. Umstattd, "Improved electrostatic design for MILO cathodes," *IEEE Trans. Plasma Sci.*, vol. 30, no. 3, pp. 992–997, Jun. 2002, doi: 10.1109/TPS.2002.801550.

[19] M. D. Haworth et al., "Comprehensive diagnostic suite for a magnetically insulated transmission line oscillator," *Rev. Sci. Instrum.*, vol. 71, no. 3, pp. 1539–1547, Mar. 2000, doi: 10.1063/1.1150500.

[20] M. Haworth et al., "Recent progress in the hard-tube MILO experiment," *Proc. SPIE*, vol. 3185, p. 28, Oct. 1997, doi: 10.1117/12.279433.

[21] S. E. Calico, M. C. Clark, R. W. Lemke, and M. C. Scott, "Experimental and theoretical investigations of a magnetically insulated line oscillator (MILO)," *Proc. SPIE*, vol. 2557, pp. 50–59, Sep. 1995, doi: 10.1117/12.218591.

[22] D. A. Packard et al., "HFSS and CST simulations of a GW-class MILO," *IEEE Trans. Plasma Sci.*, vol. 48, no. 6, pp. 1894–1901, Jun. 2020, doi: 10.1109/TPS.2020.2990163.

[23] T. Jiang, J. Zhang, J. He, Z. Li, and J. Ling, "Experimental research on Ku-band magnetically insulated transmission line oscillator," *Phys. Plasmas*, vol. 22, no. 10, Oct. 2015, Art. no. 102112, doi: 10.1063/1.4933351.

[24] D. H. Kim, H. C. Jung, S. H. Min, S. H. Shin, and G. S. Park, "Dynamics of mode competition in a gigawatt-class magnetically insulated line oscillator," *Appl. Phys. Lett.*, vol. 90, no. 12, Mar. 2007, Art. no. 124103, doi: 10.1063/1.2714992.

[25] V. Nallasamy, S. K. Datta, S. U. Reddy, and P. K. Jain, "Advances and present trends in magnetically insulated line oscillator," *J. Electromagn. Waves Appl.*, vol. 31, no. 17, pp. 1864–1874, Nov. 2017, doi: 10.1080/09205071.2017.1338622.

[26] R. Cousin, J. Larour, P. Gouard, and P. Raymond, "Evidence of the $3\pi/4$ interaction mode in a compact magnetically insulated line oscillator process," *J. Appl. Phys.*, vol. 100, no. 8, Oct. 2006, Art. no. 084512, doi: 10.1063/1.2357645.

[27] Y. Yu, X. Wang, Y. Fan, A. Li, and S. Li, "Design of a dual-band radiation system for a complex magnetically insulated line oscillator," *AIP Adv.*, vol. 8, no. 5, May 2018, Art. no. 055212, doi: 10.1063/1.5027116.

[28] Y. Fan, S. Li, X. Wang, A. Li, Y. Yu, and Z. Liu, "Influence of voltage rise time on operation frequency in magnetically insulated transmission line oscillator," *Rev. Sci. Instrum.*, vol. 90, no. 4, Apr. 2019, Art. no. 044704, doi: 10.1063/1.5080514.

[29] H. Xu, X.-Y. Wang, Y.-W. Fan, A. Li, and Z. Liu, "A high-efficiency ridged magnetically insulated transmission line oscillator," *IEEE Trans. Electron Devices*, vol. 67, no. 10, pp. 4442–4446, Oct. 2020, doi: 10.1109/TED.2020.3013726.

[30] G. Dixit, A. Kumar, and P. K. Jain, "Design analysis and simulation study of an efficiency enhanced L-band MILO," *Phys. Plasmas*, vol. 24, no. 1, Jan. 2017, Art. no. 013113, doi: 10.1063/1.4973929.

[31] V. Nallasamy, S. K. Datta, S. U. Reddy, and P. K. Jain, "Efficiency enhancement of an S-band magnetically insulated line oscillator," *Int. J. Microw. Opt. Technol.*, vol. 11, no. 5, pp. 324–331, Sep. 2016.

[32] J. C. Slater, *Microwave Electronics*. New York, NY, USA: Van Nostrand, 1951.

[33] G. B. Collins, *Microwave Magnetrons*. New York, NY, USA: McGraw-Hill, 1948.

[34] E. Okress, *Crossed-Field Microwave Devices*. New York, NY, USA: Academic, 1961.

[35] J. R. M. Vaughan, "A model for calculation of magnetron performance," *IEEE Trans. Electron Devices*, vol. ED-20, no. 9, pp. 818–826, Sep. 1973, doi: 10.1109/T-ED.1973.17750.

[36] A. A. Kim, B. M. Kovalchuk, E. V. Kumpjak, and A. N. Zoi, "0.75 MA, 400 ns rise time LTD stage," in *12th IEEE Int. Pulsed Power Conf. Dig. Tech. Papers*, vol. 2, Jun. 1999, pp. 955–958, doi: 10.1109/PPC.1999.823675.

[37] R. M. Gilgenbach et al., "MAIZE: A 1 MA LTD-driven Z-pinch at the University of Michigan," *AIP Conf.*, vol. 1088, no. 1, pp. 259–262, Jan. 2009, doi: 10.1063/1.3079742.

[38] R. D. McBride et al., "A Primer on pulsed power and linear transformer drivers for high energy density physics applications," *IEEE Trans. Plasma Sci.*, vol. 46, no. 11, pp. 3928–3967, Nov. 2018, doi: 10.1109/TPS.2018.2870099.

[39] M. G. Mazarakis et al., "High-current linear transformer driver development at Sandia National Laboratories," *IEEE Trans. Plasma Sci.*, vol. 38, no. 4, pp. 704–713, Apr. 2010, doi: 10.1109/TPS.2009.2035318.

[40] L. Brillouin, "Theory of the magnetron. I," *Phys. Rev.*, vol. 60, no. 5, pp. 385–396, Sep. 1941, doi: 10.1103/PhysRev.60.385.

[41] L. Brillouin, "Theory of the magnetron. III," *Phys. Rev.*, vol. 63, nos. 3–4, pp. 127–136, Feb. 1943, doi: 10.1103/PhysRev.63.127.

[42] L. Brillouin, "A theorem of Larmor and its importance for electrons in magnetic fields," *Phys. Rev.*, vol. 67, nos. 7–8, pp. 260–266, Apr. 1945, doi: 10.1103/PhysRev.67.260.

[43] G. D. Sims, "Preoscillation phenomena in space-charge clouds below the main oscillation threshold," in *Crossed-Field Microwave Devices*. New York, NY, USA: Academic, 1961, pp. 179–208.

[44] O. Buneman, "Symmetrical states and their breakup," in *Crossed-Field Microwave Devices*, New York, NY, USA: Academic, 1961, pp. 209–233.

[45] R. C. Davidson, *Physics of Nonneutral Plasmas*. Redwood City, CA, USA: Addison-Wesley, 1990.

[46] R. C. Davidson, G. L. Johnston, K. T. Tsang, and A. T. Drobot, "Cylindrical Brillouin flow in relativistic smooth-bore magnetrons," *Proc. SPIE*, vol. 1061, pp. 186–200, Jul. 1989, doi: 10.1117/12.951796.

[47] T. M. Antonsen and E. Ott, "Theory of intense ion beam acceleration," *Phys. Fluids*, vol. 19, no. 1, pp. 52–59, Jan. 1976, doi: 10.1063/1.861327.

[48] E. Ott and R. V. Lovelace, "Magnetic insulation and microwave generation," *Appl. Phys. Lett.*, vol. 27, no. 7, pp. 378–380, Oct. 1975, doi: 10.1063/1.88499.

[49] J. M. Creedon, "Relativistic Brillouin flow in the high ν/γ diode," *J. Appl. Phys.*, vol. 46, no. 7, pp. 2946–2955, Jul. 1975, doi: 10.1063/1.322034.

[50] J. M. Creedon, "Magnetic cutoff in high-current diodes," *J. Appl. Phys.*, vol. 48, no. 3, pp. 1070–1077, Mar. 1977, doi: 10.1063/1.323782.

[51] C. W. Mendel, D. B. Seidel, and S. E. Rosenthal, "A simple theory of magnetic insulation from basic physical considerations," *Laser Part. Beams*, vol. 1, no. 3, pp. 311–320, Aug. 1983, doi: 10.1017/S0263034600000379.

[52] P. J. Christenson, D. P. Chernin, A. L. Garner, and Y. Y. Lau, "Resistive destabilization of cycloidal electron flow and universality of (near-) Brillouin flow in a crossed-field gap," *Phys. Plasmas*, vol. 3, no. 12, pp. 4455–4462, Dec. 1996, doi: 10.1063/1.872064.

[53] P. J. Christenson and Y. Y. Lau, "One-dimensional modulational instability in a crossed-field gap," *Phys. Rev. Lett.*, vol. 76, no. 18, pp. 3324–3327, Apr. 1996, doi: 10.1103/PhysRevLett.76.3324.

[54] A. L. Garner, Y. Y. Lau, and D. Chernin, "Collapse of cycloidal electron flows induced by misalignments in a magnetically insulated diode," *Phys. Plasmas*, vol. 5, no. 6, pp. 2447–2453, Jun. 1998, doi: 10.1063/1.872921.

[55] M. Lopez, Y. Y. Lau, J. W. Luginsland, D. W. Jordan, and R. M. Gilgenbach, "Limiting current in a relativistic diode under the condition of magnetic insulation," *Phys. Plasmas*, vol. 10, no. 11, pp. 4489–4493, Nov. 2003, doi: 10.1063/1.1613654.

[56] A. Palevsky, "Generation of intense microwave radiation by the relativistic e-beam magnetron (experiment and numerical simulation)," Ph.D. dissertation, Massachusetts Inst. Technol., Cambridge, MA, USA, 1980. Accessed: Apr. 14, 2021. [Online]. Available: https://dspace.mit.edu/handle/1721.1/16050

[57] A. Palevsky, G. Bekefi, and A. T. Drobot, "Numerical simulation of oscillating magnetrons," *J. Appl. Phys.*, vol. 52, no. 8, pp. 4938–4941, Aug. 1981, doi: 10.1063/1.329381.

[58] D. H. Simon, Y. Y. Lau, J. W. Luginsland, and R. M. Gilgenbach, "An unnoticed property of the cylindrical relativistic Brillouin flow," *Phys. Plasmas*, vol. 19, no. 4, Apr. 2012, Art. no. 043103, doi: 10.1063/1.3701705.

[59] D. H. Simon, Y. Y. Lau, G. Greening, P. Wong, B. Hoff, and R. M. Gilgenbach, "Stability of Brillouin flow in the presence of slow-wave structure," *Phys. Plasmas*, vol. 23, no. 9, Sep. 2016, Art. no. 092101, doi: 10.1063/1.4961917.

[60] P. F. Ottinger and J. W. Schumer, "Rescaling of equilibrium magnetically insulated flow theory based on results from particle-in-cell simulations," *Phys. Plasmas*, vol. 13, no. 6, Jun. 2006, Art. no. 063109, doi: 10.1063/1.2212831.

[61] O. Buneman, R. H. Levy, and L. M. Linson, "Stability of crossed-field electron beams," *J. Appl. Phys.*, vol. 37, no. 8, pp. 3203–3222, Jul. 1966, doi: 10.1063/1.1703185.

[62] J. Swegle and E. Ott, "Instability of the Brillouin-flow equilibrium in magnetically insulated structures," *Phys. Rev. Lett.*, vol. 46, no. 14, pp. 929–932, Apr. 1981, doi: 10.1103/PhysRevLett.46.929.

[63] T. M. Antonsen, E. Ott, C. L. Chang, and A. T. Drobot, "Parametric scaling of the stability of relativistic laminar flow magnetic insulation," *Phys. Fluids*, vol. 28, no. 9, pp. 2878–2881, Sep. 1985, doi: 10.1063/1.865208.

[64] R. C. Davidson, H.-W. Chan, C. Chen, and S. Lund, "Equilibrium and stability properties of intense non-neutral electron flow," *Rev. Mod. Phys.*, vol. 63, no. 2, pp. 341–374, Apr. 1991, doi: 10.1103/RevModPhys.63.341.

[65] K. T. Tsang and R. C. Davidson, "Macroscopic cold-fluid equilibrium properties of relativistic non-neutral electron flow in a cylindrical diode," *Phys. Rev. A, Gen. Phys.*, vol. 33, no. 6, pp. 4284–4292, Jun. 1986, doi: 10.1103/physreva.33.4284.

[66] P. H. Stoltz, J. W. Luginsland, A. Chap, D. N. Smithe, and J. R. Cary, "A new simple algorithm for space charge limited emission," *Phys. Plasmas*, vol. 27, no. 9, Sep. 2020, Art. no. 093103, doi: 10.1063/5.0020781.

[67] D. Chernin, A. Jassem, and Y. Y. Lau, "Thermal electron flow in a planar crossed-field diode," *IEEE Trans. Plasma Sci.*, vol. 48, no. 9, pp. 3109–3114, Sep. 2020, doi: 10.1109/TPS.2020.3017715.

[68] A. Jassem, "Analysis of non-uniform cathode emission and backward wave oscillations in a traveling wave tube," Ph.D. dissertation, Univ. Michigan, Ann Arbor, MI, USA, 2021.

[69] Y. Y. Lau, J. W. Luginsland, K. L. Cartwright, D. H. Simon, W. Tang, B. W. Hoff, and R. M. Gilgenbach, "A re-examination of the Buneman–Hartree condition in a cylindrical smooth-bore relativistic magnetron," *Phys. Plasmas*, vol. 17, no. 3, Mar. 2010, Art. no. 033102, doi: 10.1063/1.3328804.

[70] R. L. Walker, in *Microwave Magnetrons*, G. B. Collins, Ed. New York, NY, USA: McGraw-Hill, 1948, p. 227.

[71] D. A. Packard, "Innovative crossed-field devices for the generation of high power microwaves," Ph.D. dissertation, Univ. Michigan, Ann Arbor, MI, USA, 2021.

[72] D. A. Packard, Y. Y. Lau, C. J. Swenson, N. M. Jordan, E. Guerin, and R. M. Gilgenbach, "Experiments on a 10 kA, 240 kV magnetically insulated line oscillator (MILO)," presented at the IEEE Int. Conf. Plasma Sci., Sep. 2021.

[73] D. H. Simon, "Equilibrium and stability of Brillouin flow in planar, conventional, and inverted magnetrons," Ph.D. dissertation, Univ. Michigan, Ann Arbor, MI, USA, 2016.

[74] T. P. Fleming, M. R. Lambrecht, and K. L. Cartwright, "Numerical simulations of a relativistic inverted magnetron," *IEEE Trans. Plasma Sci.*, vol. 38, no. 7, pp. 1563–1573, Jul. 2010, doi: 10.1109/TPS.2010.2048209.

[75] Y. Y. Lau, "The Child-Langmuir law and the physics of diodes," plenary paper, presented at the IEEE Int. Conf. Plasma Sci., Virtual, Dec. 2020.

[76] P. Zhang, Á. Valfells, L. K. Ang, J. W. Luginsland, and Y. Y. Lau, "100 years of the physics of diodes," *Appl. Phys. Rev.*, vol. 4, no. 1, Mar. 2017, Art. no. 011304, doi: 10.1063/1.4978231.

[77] P. Zhang, Y. S. Ang, A. L. Garner, Á. Valfells, J. W. Luginsland, and L. K. Ang, "Space–charge limited current in nanodiodes: Ballistic, collisional, and dynamical effects," *J. Appl. Phys.*, vol. 129, no. 10, Mar. 2021, Art. no. 100902, doi: 10.1063/5.0042355.

[78] D. Chernin, Y. Y. Lau, J. J. Petillo, S. Ovtchinnikov, D. Chen, A. Jassem, R. Jacobs, D. Morgan, and J. H. Booske, "Effect of nonuniform emission on Miram curves," *IEEE Trans. Plasma Sci.*, vol. 48, no. 1, pp. 146–155, Jan. 2020, doi: 10.1109/TPS.2019.2959755.

[79] A. Jassem, D. Chernin, J. J. Petillo, Y. Y. Lau, A. Jensen, and S. Ovtchinnikov, "Analysis of anode current from a thermionic cathode with a 2-D work function distribution," *IEEE Trans. Plasma Sci.*, vol. 49, no. 2, pp. 749–755, Feb. 2021, doi: 10.1109/TPS.2020.3048097.

[80] J. D. Jackson, *Classical Electrodynamics*. New York, NY, USA: Wiley, 1962.

Y. Y. Lau (Fellow, IEEE) received the B.S., M.S., and Ph.D. degrees in electrical engineering from the Massachusetts Institute of Technology (MIT), Cambridge, MA, USA, in 1968, 1970, and 1973, respectively.

He was an Instructor and then an Assistant Professor in applied mathematics with MIT from 1973 to 1979, and a Research Physicist with Science Applications, Inc., McLean, VA, USA, from 1980 to 1983, and the U.S. Naval Research Laboratory, Washington, DC, USA, from 1983 to 1992. He has been a Professor with the University of Michigan, Ann Arbor, MI, USA, since 1992. He has supervised or co-supervised 32 Ph.D. students. He has worked on electron beams, coherent radiation sources, plasmas, and discharges.

Dr. Lau was a Fellow of the American Physical Society in 1986. He was a recipient of the IEEE Plasma Science and Applications Award in 1999 and the IEEE John R. Pierce Award for Excellence in Vacuum Electronics in 2017. He served three terms as an Associate Editor for *Physics of Plasmas* from 1994 to 2002.

Drew A. Packard (Member, IEEE) received the B.S.E., M.S.E., and Ph.D. degrees in nuclear engineering and radiological sciences from the University of Michigan, Ann Arbor, MI, USA, in 2016, 2017, and 2021, respectively.

As a graduate student, he performs research on high-power microwave (HPM) devices under the mentorship of Prof. Gilgenbach with the Plasma, Pulsed Power, and Microwave Laboratory (PPPML), University of Michigan, specializing in crossed field devices. During his time with PPPML, he has simulated, designed, and tested magnetrons, crossed field amplifiers, and magnetically insulated line oscillators (MILOs). He has completed two internships with the L-3 Communications, Electron Devices Division, San Carlos, CA, USA. His general research interests include charged particle beams, accelerators, diode physics, beam–wave interaction, RF sources and engineering, antennas, HPMs, pulsed power, simulation techniques, and general electromagnetic phenomena.

Christopher J. Swenson (Student Member, IEEE) received the B.S.E. and M.S.E. degrees in nuclear engineering and radiological sciences from the University of Michigan, Ann Arbor, MI, USA, in 2018 and 2019, respectively, where he is currently pursuing the Ph.D. degree with the Plasma, Pulsed Power, and Microwave Laboratory.

His research focuses on high-power microwave devices including crossed-field amplifiers, magnetrons, and magnetically insulated line oscillators (MILOs).

John W. Luginsland (Fellow, IEEE) received the B.S.E., M.S.E., and Ph.D. degrees in nuclear engineering from the University of Michigan, Ann Arbor, MI, USA, in 1992, 1994, and 1996, respectively.

He was a Staff Member at the Directed Energy Directorate of the Air Force Research Laboratory (AFRL), Kirtland AFB, NM, USA, in the late 1990s, having first joined AFRL as a National Research Council Post-Doctoral Fellow. He has industrial experience at Confluent Sciences, LLC, Albuquerque, NM, USA; NumerEx, LLC, Ithaca, NY, USA; and Science Applications International Corporation, Albuquerque. He also has academic experience as a Professor with the Department of Computational Mathematics, Science and Engineering and the Department of Electrical and Computer Engineering, Michigan State University, East Lansing, MI, USA. He is currently the Program Officer of plasma and electro-energetic physics and a member of the Chief Scientist's Technical Advisory Council with the Air Force Office of Scientific Research (AFOSR), Arlington, VA, USA. In previous terms of government service, he worked as an Acting Division Chief, a Division Technical Advisor, an Acting Branch Chief, and the Program Officer of plasma physics from 2009 to 2014, and lasers and optics from 2014 to 2017 with AFOSR. From 2013 to 2014, he was the Program Element Monitor and an Action Officer of Air Force Basic Research in the Office of the Assistant Secretary of the Air Force for Acquisitions (SAF/AQR).

Dr. Luginsland is a fellow of the Air Force Research Laboratory. He received the 2006 IEEE Nuclear and Plasma Science Society's Early Achievement Award. He was the elected Vice-Chair of the IEEE's Plasma Science and Applications Committee and a Co-Chair on a National Academy consensus study "Powering the Army of the Future." He also served as a member for the Intelligence Science and Technology Experts Group (ISTEG), National Academies of Science, Engineering, and Medicine, Washington, DC, USA.

Dion Li (Student Member, IEEE) is currently pursuing the B.S.E. degree in engineering physics with the University of Michigan, Ann Arbor, MI, USA.

His research interests include electromagnetic theory, crossed-field diodes, and plasma wakefield acceleration.

Abhijit Jassem received the B.S. degree in nuclear engineering from Purdue University, West Lafayette, IN, USA, in 2016, and the Ph.D. degree from the University of Michigan's Nuclear Engineering and Radiological Sciences Department, Ann Arbor, MI, USA, in 2021.

He worked with the Plasma, Pulsed Power, and Microwave Laboratory, University of Michigan. He is currently working at Niowave, Inc., Lansing, MI, USA.

Nicholas M. Jordan (Senior Member, IEEE) received the B.S.E., M.S.E., and Ph.D. degrees in nuclear engineering and radiological science from the University of Michigan, Ann Arbor, MI, USA, in 2002, 2004, and 2008, respectively.

From 2008 to 2013, he was with Cybernet Systems, Ann Arbor, MI, where he developed technology to disable uncooperative vehicles using microwave pulses. He is currently an Associate Research Scientist with the Plasma, Pulsed Power, and Microwave Laboratory, University of Michigan. His current research interests include pulsed power, laser ablation, Z-pinch physics, plasma discharges, magnetrons, magnetically insulated line oscillators (MILOs), crossed-field amplifiers (CFAs), and other high-power microwave devices.

Ryan D. McBride (Member, IEEE) received the Ph.D. degree from Cornell University, Ithaca, NY, USA, in 2009, where he conducted experimental research using the 1-MA COBRA pulsed-power facility to generate and study high-power X-ray sources.

From 2008 to 2016, he was with Sandia National Laboratories, Albuquerque, NM, USA, where he held appointments as a Staff Physicist and a Department Manager. At Sandia, he conducted research in nuclear fusion, high-power radiation generation, and high-pressure material properties using the 25-MA Z-pulsed-power facility. Since August 2016, he has been an Associate Professor with the Department of Nuclear Engineering and Radiological Sciences, University of Michigan, Ann Arbor, MI, USA. In May 2021, he became the Director of the University's Plasma, Pulsed Power, and Microwave Laboratory, which includes the MAIZE and BLUE linear transformer driver facilities. His research interests include plasma physics, nuclear fusion, high-power radiation generation, pulsed-power technology, and diagnostics.

Ronald M. Gilgenbach (Life Fellow, IEEE) received the B.S. and M.S. degrees from the University of Wisconsin, Madison, WI, USA, in 1972 and 1973, respectively, and the Ph.D. degree in electrical engineering from Columbia University, New York City, NY, USA, in 1978.

He is the Chihiro Kikuchi Collegiate Professor in the Nuclear Engineering and Radiological Sciences Department at the University of Michigan (UM), Ann Arbor, MI, USA. In the mid-1970s, he spent several years as a Member of the Technical Staff at Bell Telephone Labs, Holmdel, NJ, USA. From 1978 to 1980, he performed gyrotron research at the Naval Research Laboratory (NRL), Washington, DC, USA, and conducted the first electron cyclotron heating experiments on a tokamak plasma at the Oak Ridge National Laboratory, Oak Ridge, TN, USA. He joined the faculty of UM in 1980, where he founded the Plasma, Pulsed Power and Microwave Laboratory. At UM, he has supervised/co-supervised 52 graduated Ph.D. students. He has some 200 publications in refereed journals and book chapters and five U.S. patents.

Prof. Gilgenbach is a fellow of the American Physical Society Division of Plasma Physics and the American Nuclear Society. He received the IEEE Plasma Science and Applications Committee (PSAC) Award in 1997 and the IEEE Peter Haas Pulsed Power Award in 2017. He served as the IEEE PSAC Chair from 2007 to 2008.